Key Points:
- Active hydrothermal chimneys were discovered at Alarcón Rise and Pescadero Basin in high-resolution AUV data and sampled on ROV dives
- Black smoker fluids and sulfide-rich deposits from Alarcón Rise resemble other basalt-hosted fields
- Pescadero Basin fluids have interacted with sediment to produce hydrocarbons and have built chimneys and mounds of calcite with little sulfide

Supporting Information:
- Supporting Information S1
- Table S1
- Table S2
- Figure S1
- Figure S2
- Figure S3

Correspondence to:
J. B. Paduan,
paje@mbari.org

Discovery of Hydrothermal Vent Fields on Alarcón Rise and in Southern Pescadero Basin, Gulf of California

Jennifer B. Paduan[1], Robert A. Zierenberg[2], David A. Clague[1], Ronald M. Spelz[3], David W. Caress[1], Giancarlo Troni[4], Hans Thomas[1], Justin Glessner[2], Marvin D. Lilley[5], Thomas Lorenson[6], John Lupton[7], Florian Neumann[8], Miguel A. Santa Rosa-del Rio[3], and C. Geoffrey Wheat[9]

[1]Monterey Bay Aquarium Research Institute, Moss Landing, CA, USA, [2]Earth and Planetary Sciences, University of California, Davis, CA, USA, [3]Departamento de Geología, Facultad de Ciencias Marinas, Universidad Autónoma de Baja California, Ensenada, Mexico, [4]Department of Mechanical and Metallurgical Engineering, Pontificia Universidad Católica de Chile, Santiago, Chile, [5]School of Oceanography, University of Washington, Seattle, WA, USA, [6]U.S. Geological Survey, Santa Cruz, CA, USA, [7]Hatfield Marine Science Center, PMEL, NOAA, Newport, OR, USA, [8]Centro de Investigación Científica y de Educación Superior de Ensenada, Ensenada, Mexico, [9]University of Alaska Fairbanks, Moss Landing, CA, USA

Abstract Hydrothermal vent fields located in the gap between known sites in Guaymas Basin and 21°N on the East Pacific Rise were discovered on the Alarcón Rise and in southern Pescadero Basin. The Alarcón Rise spreading segment was mapped at 1-m resolution by an autonomous underwater vehicle. Individual chimneys were identified using the bathymetric data. Vent fields were interpreted as active from temperature anomalies in water column data and observed and sampled during remotely operated vehicle dives. The Ja Sít, Pericú, and Meyibó active fields are near the eruptive fissure of an extensive young lava flow. Vent fluids up to 360 °C from Meyibó have compositions similar to northern East Pacific Rise vents. The Tzab-ek field is 850 m west of the volcanic axis, and active chimneys rise up to 33 m above a broad sulfide mound. The inactive field is 10 km north-northeast along the rift axis, and most sulfide chimneys are enriched in Zn and associated elements that are transported at lower temperature compared to the more Cu-rich active fields. In southern Pescadero Basin, the Auka field is on the margin of a sediment-filled graben at 3,670-m depth. Discharging fluids are clear, contain hydrocarbons, and have neutral pH, elevated salinity, and temperatures up to 291 °C. They have deposited massive mounds of calcite with minor sulfide. The fluids are compositionally similar to those in Guaymas Basin, produced by high-temperature basalt-seawater interaction followed by reaction with sediment. The paucity of sulfide minerals suggests subsurface deposition of metals.

Plain Language Summary Hydrothermal chimneys on two previously unexplored spreading ridges, the Alarcón Rise and southern Pescadero Basin, were discovered on Monterey Bay Aquarium Research Institute expeditions to the Gulf of California. Autonomous underwater vehicles were used to map the region, followed by dives with remotely operated vehicles to observe and sample features on the seafloor. Many of the chimneys on the Alarcón Rise were found to be high-temperature *black smokers*, so-called because of the particles of metal-sulfide that precipitate from the hot fluid as it cools. Deposited precipitates have built chimneys up to 33 m tall, composed of iron, copper, and zinc sulfides, and include some precious metals. The venting fluid was seawater that has been heated by, and interacted with, underlying basalt lavas through which it circulated. In the southern Pescadero Basin, hydrothermal fluids are clear and somewhat cooler than at the Alarcón Rise, and the chimneys are composed of calcite with little sulfide. These fluid and deposit compositions are most similar to those at the Guaymas Basin, located farther north in the Gulf of California, where the heated vent fluids pass through, and react with, thick sediments before exiting the seafloor.

1. Introduction

Hydrothermal venting is widespread along the global mid-ocean ridge system and is the primary process cooling newly formed ocean crust (Stein et al., 1995). Venting results in significant fluxes of heat, fluids, gases, and chemicals between the lithosphere and seawater. Most known hydrothermal vents occur on volcanic substrate with minimal sediment cover. The hot, acidic fluids are rich in dissolved metals, and when they mix with cold seawater they precipitate polymetallic sulfides that build chimneys and mounds. The

AGU
100
ADVANCING EARTH
AND SPACE SCIENCE

Geochemistry, Geophysics, Geosystems

10.1029/2018GC007771

deposits usually contain Fe, Zn, Cu, and an array of minor elements, many of which have economic importance. Hydrothermal vent sites that occur on sediment-covered spreading centers are less common. (Koski et al., 1993; Zierenberg et al., 1998). Hydrothermal chimneys in Guaymas Basin in the Gulf of California are enriched in carbonate relative to other sediment-covered vent fields (Von Damm, 1990).

Active vent sites were generally located using ship-based hydrocasts and tow-yos with conductivity, temperature, pressure (for depth; CTD), Eh, and particle sensors to search for anomalies (plumes) in the water column that indicate proximity to active chimneys (e.g., Baker et al., 1995). Before high-resolution mapping was available, once anomalies had been located, towed camera systems or dives using manned submersibles or remotely operated vehicles (ROVs) refined the search for the active vents. These searches commonly relied on observations of dispersed hydrothermal sediment or near-vent animals such as sponges or serpulid worms and required that the dives closely approach the vents in order to locate them. The process was commonly time-consuming, could miss chimneys outside the field of view, and did not locate inactive chimney fields.

Recent advances in high-resolution mapping from autonomous underwater vehicles (AUVs) have streamlined the search process. The bathymetry produced by such vehicles can resolve hydrothermal chimneys and mounds that are only a few meters across and high, whether they are active or inactive (Connelly et al., 2012; Jamieson et al., 2014; Nakamura et al., 2013) and map uplifted sediment hills where the cooling of sills beneath might drive fluid circulation (Clague et al., 2018; Zierenberg et al., 2015). Water property data (e.g., conductivity, temperature, and particles) are collected concurrently with the bathymetric data. Subsequent ROV dives can focus immediately on the most likely targets for hydrothermal fluid, deposit, and biological sampling.

These techniques were utilized by the Monterey Bay Aquarium Research Institute (MBARI) to discover and sample hydrothermal systems at Axial Seamount (Clague et al., 2013) and Endeavour Ridge (Jamieson et al., 2014). In both cases, the presence of nearby vents was known and essential to focusing the AUV search, and new chimneys were discovered by expanding the explored areas. Here we apply these techniques to the Alarcón Rise and in the southern Pescadero Basin, which are mid-ocean ridge segments in the southern Gulf of California that had no known hydrothermal activity. Mapping the entire ridge segment and basin with an AUV provides an inventory and distribution of current and past hydrothermal activity and led to discovery of six active and one inactive hydrothermal fields. Samples of discharging fluids and chimney materials were subsequently collected on ROV dives that located the chimneys within minutes of reaching the seafloor. The mapping and chemical data from these inactive chimneys and active vent sites provide constraints on the geological setting, fluid and deposit chemistry, and the geochemical reactions that support diverse assemblages of vent fauna (Goffredi et al., 2017).

1.1. Geological Setting and Prior Work

The Gulf of California is a transtensional plate boundary characterized by divergent right-lateral shear between the Pacific and North American plates (Figure 1a). Seafloor spreading began in the Gulf of California ~3.5 Ma when the Baja Peninsula rifted from the mainland of Mexico (Lizarralde et al., 2007, and references therein). Of the segments accommodating that spreading, the Alarcón Rise is the longest, at 50 km. It lies at the mouth of the gulf between the southern tip of the Baja Peninsula and the mainland of Mexico (Figure 1a). Its full spreading rate is about 49 mm/year (DeMets et al., 2010), which accounts for nearly 92% of the relative motion between the Pacific and North American tectonic plates (Lizarralde et al., 2007). The axis of the ridge ranges from about −2,200- to −2,400-m deep. It is the northernmost segment of the East Pacific Rise (EPR) that is not buried beneath continental sediment over its length.

At its southwestern end, the Alarcón Rise is bounded by the ~60-km-long Tamayo Transform Fault, which connects to the 21°N segment of the EPR, an intermediate-spreading rate segment. South from there almost to Antarctica, intermediate to ultra-fast-spreading, sediment-starved ridge segments of the EPR offset by transform faults characterize the plate boundary between the Pacific Plate and the tectonic plates to its east. Hydrothermal systems are known from many of those segments (Beaulieu et al., 2013; Von Damm, 1990, 1995). The nearest is 275 km SSW of the Alarcón Rise at 21°N (Figure 1a; Francheteau et al., 1979; Spiess et al., 1980). Its hydrothermal system resembles others on the EPR, with black smokers building metal-sulfide-rich chimneys (Von Damm, Edmond, Grant, et al., 1985; Zierenberg et al., 1984).
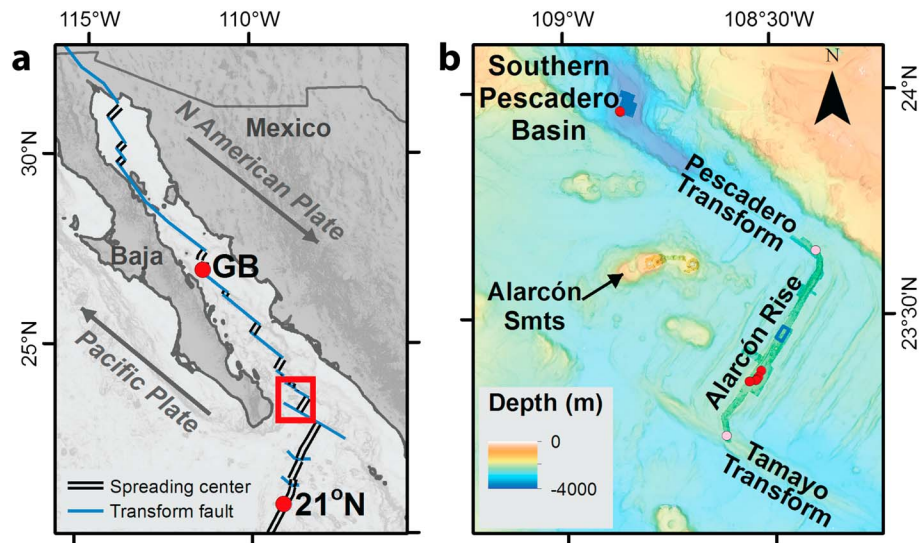
Figure 1. (a) Map of Gulf of California, showing tectonics of the region and the study area in the red box. Neighboring hydrothermal vent sites are red circles: GB, Guaymas Basin; 21°N, the 21°N site on the EPR. (b) Autonomous underwater vehicle (AUV) survey coverage is shown over ship-collected and satellite bathymetry (faded; Wessel, 2008). The Tamayo and Pescadero Transform Faults bound the Alarcón Rise and southern Pescadero Basin spreading ridges. The new hydrothermal vent sites discussed here are located at the red dots, and the inactive chimney field in Figure 8 is within the blue rectangle. Low-temperature seeps discovered on the transforms are pink dots (Clague et al., 2018). All maps are in the UTM zone 12°N coordinate system.

At the northeast end of the Alarcón Rise, the plate boundary enters the Gulf of California and becomes dominated by a system of right-stepping, right-lateral transform faults connecting a series of short spreading segments blanketed with thick terrigenous and biogenic sediment (Lonsdale et al., 1980). At the northern end of the gulf the San Andreas Fault begins, and the plate boundary becomes almost exclusively transform (Figure 1a).

The nearest of these spreading segments to the Alarcón Rise is the ~3,800-m-deep southern Pescadero Basin (Figure 1b), 60 km NW along the Pescadero Transform Fault. It is one of a series of three grabens offset by transform faults collectively named the Pescadero Basin and located 150 km east of La Paz, Mexico.

The Guaymas Basin is about 400 km further NW of the Pescadero Basin (Figure 1a) and is where the only previously known active high-temperature hydrothermal venting within the Gulf of California occurs. It is a sediment-filled spreading basin (Lonsdale et al., 1980), with more compositional diversity than EPR hydrothermal sites due to interaction of hot fluids with thick sediments. Chimneys in Guaymas Basin include black smokers, but also white chimneys built primarily of calcite and anhydrite that emit cloudy or clear, high-alkalinity and hydrocarbon-rich fluids (Berndt et al., 2016; Peter & Scott, 1988; Simoneit et al., 1986; Von Damm, Edmond, Measures, & Grant, 1985). Vent fauna also are different in the Guaymas Basin than on the EPR (Goffredi et al., 2017, and references therein).

Hydrothermal vent sites were not previously known between the 21°N EPR and the Guaymas Basin sites, a gap of more than 750 km (Figure 1a). MBARI conducted two ROV dives in 2003 on the Alarcón Rise to search for hydrothermal activity and collect associated fauna, but without high-resolution maps the search was unsuccessful. In 2012, MBARI mapped at 1-m resolution the entire length of the neo-volcanic zone and onto the adjacent transforms using the AUV *D. Allan B.* from the R/V *Zephyr* and potential chimney fields were identified (Figure 1b). Days later, the R/V *Western Flyer* followed, and guided by the maps, the ROV *Doc Ricketts* approached the first active vent field 20 min after reaching the seafloor.

MBARI returned in spring 2015 with the R/V *Rachel Carson* and the AUV to increase the mapped coverage of the Alarcón Rise and map in the southern Pescadero Basin, where chimneys were identified in the AUV bathymetric data and determined to be active based on AUV CTD water-column anomalies (Caress et al., 2015). The mapping surveys were closely followed by ROV dives to sample this hydrothermal system.

2. Methods

High-resolution bathymetric mapping was conducted in 2012 and 2015 with the MBARI AUV *D. Allan B.*, a Dorado class, 0.53-m diameter vehicle that carries multibeam, side scan, and subbottom sonars and a CTD sensor (details of the vehicle, sonars, operations, and data processing with MB-System software are in Caress et al., 2008, 2012, and Clague et al., 2014). Processed AUV bathymetry for surveys run at 50-m altitude have 0.1-m vertical precision and 1-m lateral resolution. The CTD temperature data have nominal 0.002 °C precision.

AUV bathymetry and CTD data were examined for possible chimneys and hydrothermal plumes, respectively. In this environment, chimneys taller than 1.5 m are sufficiently distinctive in MB-System to allow provisional identification (supporting information Figure S1). Methods used and lessons learned from analyzing AUV and ROV data for chimneys are discussed in supporting information Text S1.

Hydrothermal activity was detected as temperature anomalies recorded by the AUV CTD due to the plumes of hot water that rise above the active vents. Following calculation of potential temperature and correcting for median local variation of potential temperature with depth, anomalies greater than 0.005 °C were identified using a spike detection filter (Caress et al., 2015). With the advance knowledge that some of the mapped chimneys were active, the ROV could be outfitted with an Omega resistance temperature detector high-temperature probe, hydraulically activated titanium major element (Ti-major) bottles, and gas-tight evacuated bottles for sampling hydrothermal vent fluids (Figure S2a) in lieu of the usual configuration to collect and stow sediment cores, lava flow samples, and some biological specimens.

ROV *Doc Ricketts* dives in 2012 and 2015 were guided by the 1-m resolution AUV maps. Large and small edifices built of hydrothermal material were considered active chimneys if fluid was emitted or microbial mat and vent-specific fauna were observed, even if the flow rate was low, and considered inactive if not. If fluid flow or vent-specific fauna were present, but not associated with a chimney, such as emitted through a crack in the rocks, it was classified as diffuse venting.

Samples collected during these dives included lavas, sediment push cores, vent fluids, and hydrothermal deposits (Clague et al., 2018). Immediately following this dive series, more intensive sampling of vent megafauna and microbes was conducted during biology dives (Figure S2; Goffredi et al., 2017). On the biology dives, temperatures were generally measured for fluids bathing the animals rather than of the hottest vent discharge. Chemical and isotopic compositions of hydrothermal fluids, precipitates, and sediments were largely determined using established techniques (Text S2). Minimum ages of lava flows underlying the vent fields were determined by ^{14}C dating of foraminifera shells sieved from the bottoms of sediment cores taken on top of the flows (Clague et al., 2013, 2014, 2018).

3. Results

3.1. Observations Based on AUV Data

#### 3.1.1. Alarcon Rise Hydrothermal Fields

Seventeen AUV surveys covered an area of ~164 km^2 along the entire 47-km length of the neovolcanic zone of the Alarcón Rise and the transitions onto the Pescadero Transform Fault to the northeast and the Tamayo Transform Fault to the southwest (Figure 1b). Surface lava flows characterize the entire length of the segment, and thick sediments are evident only along the transform faults and off-axis (Clague et al., 2018). One hundred and nine structures identified as chimneys were found along nearly 20 km of the ridge axis, and cluster in four explored and one unexplored fields that are spatially associated with the shallowest part of the ridge, and in a sixth broad group in the vicinity of a faulted volcanic cone farther north (Figure 2).

CTD data recorded during the AUV surveys had potential temperature anomalies above background variability of up to 0.13 °C near the southern end of the Meyibó chimney field (Caress et al., 2015), where ROV *Doc Ricketts* dives later confirmed the active venting of high-temperature fluids.

3.1.2. Pescadero Basin Hydrothermal Field

Two AUV surveys in the nearly 3,800-m deep southern Pescadero Basin (Figure 1b) covered 22.9 km^2, including the axis of the basin and part of the faulted western wall. No surface lava flows were evident in the area surveyed (Figure 3a), and the AUV side scan sonar indicated low acoustic backscatter throughout the floor of the basin (not shown). AUV subbottom profiles indicate that sediment thicknesses in the basin are in excess
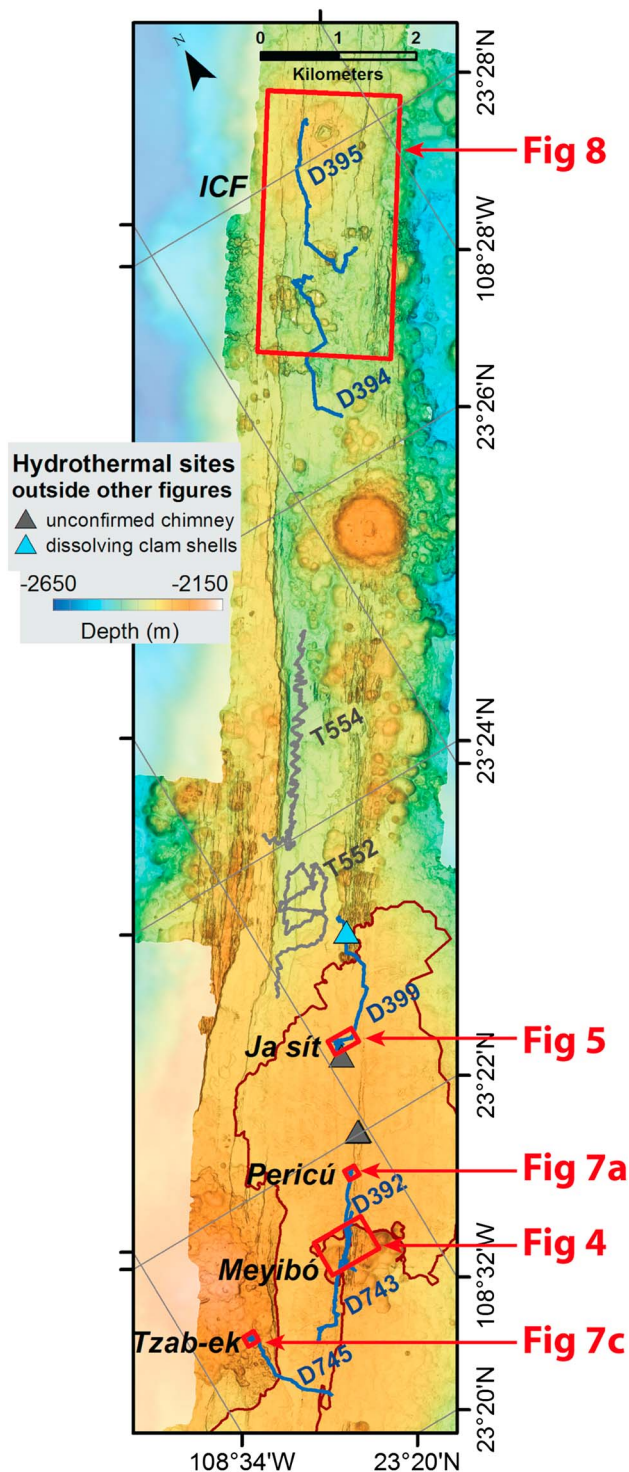
Figure 2. Map showing locations of Alarcón Rise active and inactive vent fields. Extents of maps in Figures 4, 5, 7, and 8 are red boxes. Dissolving clams interpreted to be an inactive seep site, and provisionally identified chimneys not confirmed by remotely operated vehicle (ROV) observations, that are located outside those figures are indicated with triangles. The young sheet flow along whose fissure system several of the active fields lie is partially outlined in brown. The blue lines are ROV *Doc Ricketts* dive tracks in 2012 and 2015. The gray lines are ROV *Tiburon* dive tracks in 2003, which found no hydrothermal chimneys. ICF, inactive chimney field.

of the >50-m penetration of the sonar, and thinner over tilted fault blocks (Figure 3b) and buried acoustic reflectors (Figure 3d). Mounds protrude from onlapping sediments (Figures 3c and 3d) where a cluster of chimneys is found extending for 500 m along a fault scarp that defines the southwestern edge of the rift basin, at about 3,670-m depth and 3.6 km SSW of the deepest part of the basin (Figure 3a). Hills of uplifted layered sediment disrupted by faults rise above the thick sediments filling the basin to the north of the chimneys (Figure 3a). Six small circular pits are apparent in the bathymetry (the largest is 22 m across and 8-m deep; Figure 3a; the others are <10 m across). These were not in the vicinity of the chimneys and none were investigated during ROV dives.

CTD data recorded during the AUV surveys had potential temperature anomalies above background variability of up to 0.25 °C in Pescadero Basin over and near the mapped chimneys (Caress et al., 2015). These sites were later confirmed during ROV *Doc Ricketts* dives to be actively venting high-temperature fluids.

3.2. Visual and Thermal Observations
3.2.1. Alarcón Rise Hydrothermal Fields
In 2012, 71 of the 109 identified chimney structures on the Alarcón Rise were observed on dives with the ROV *Doc Ricketts* to determine if they were active or inactive. The active hydrothermal fields are named Meyibó, Ja Sít, Pericú, and Tzab-ek from local native languages (Text S1). In 2015, 13 more of the identified chimneys on the Alarcón Rise were observed and their active/inactive status determined, and several were revisited. Hydrothermal fluids were collected from two chimneys in the Meyibó vent field. Of the 84 observed chimneys, 31 were hydrothermally active and 53 were inactive; the activity or inactivity of 25 remains unknown.

Meyibó, Pericú, and Ja Sít active vent sites are associated with the most inflated and broad part of the ridge, which is considered to be magmatically robust (Clague et al., 2018), and is located about one third of the way along the ridge from the south rather than at the midpoint. The fields are spread along 3 km of the nearly 7-km-long fissure system that erupted one of, if not the youngest lava flow on the Alarcón Rise, an extensive channelized flow partially outlined in Figure 2. This flow was dusted with sediment too thin to core for ^{14}C age dating, so is probably 50–75 years old (Clague et al., 2018). Together these fields have at least 24 active chimney structures (many have multiple spires that were not separately counted), numerous diffusely venting sites, and some inactive chimneys (Figures 2 and S2a–S2c). The vigorously active black smoker chimneys, constructed of polymetallic sulfides, grew directly on basalt at about 2,300-m depth. Lower temperature, milky-white or clear, shimmering fluids discharge from cracks in the lava (here referred to as diffuse vents). These diffuse vents and less active parts of the chimneys support lush chemosynthetic fauna, most prominently the iconic tubeworm *Riftia pachyptila* (Goffredi et al., 2017).

Meyibó chimneys and diffuse vents extend 560 m along a 30- to 50-m-wide graben cutting a group of older hummocky flows (radiocarbon dated at 1655 CE or ~365 years ago; Clague et al., 2018) that had been fractured and pulled apart ~150 m by tectonic spreading (Figure 4a). Most vents are clustered in the northern end of the field, and three are over 12 m high. The tallest chimney at Meyibó is closer to the southern end of the field
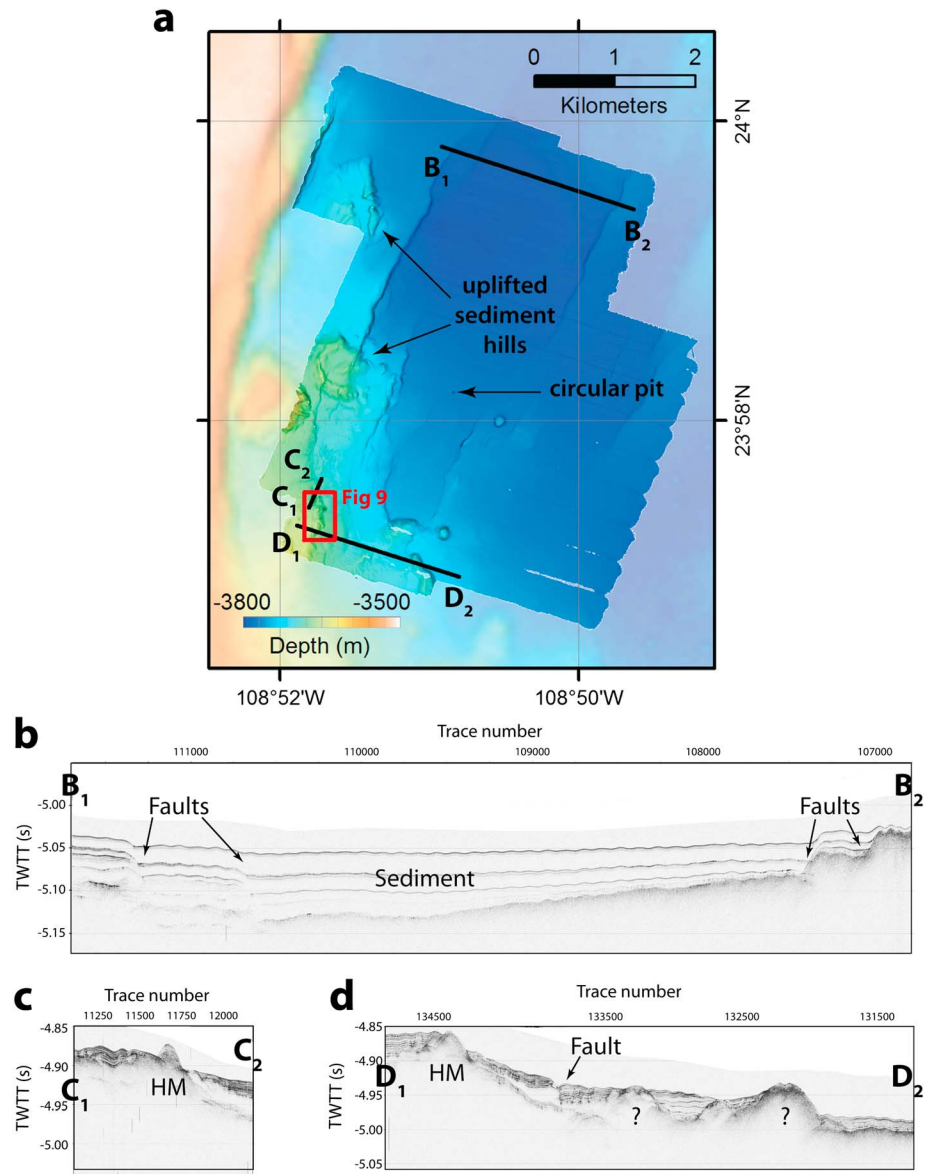
Figure 3. Southern Pescadero Basin AUV bathymetry and selected subbottom profiles. (a) Bathymetry from the two surveys superimposed over ship-collected bathymetry (faded). The Auka active vent field is within the red box, which shows the extent of the map in Figure 9. Possible uplifted sediment hills and the largest of several circular pits are identified. (b–d) AUV track lines of the subbottom profiles are black lines with the ends labeled as on the profiles. TWTT, two way travel time. (b) Subbottom profile across the basin showing normal faults on either side blanketed with thick layered sediment offset by the faults (arrows). (c) Profile across one of the hydrothermal mounds (HM) and on-lapping sediments. (d) Profile across hydrothermal mounds with onlapping layered sediment, a fault (arrow) with an acoustically transparent layer on the west side, and hard reflectors of unknown origin (labeled "?"), overlain by disrupted sediment layers.

and is 17 m high and 12 m wide at the base. ROV dives D392 in 2012 and D743 in 2015 explored the field and collected video observations and samples (Figure 4b). Fluid temperatures measured at three chimneys are up to 359 °C (Figure 4b). Fluid from a chimney in the northern cluster (Meyibó N) was collected with Ti-major and gas-tight sample bottles and from a chimney near the southern end of the field (Meyibó S) was collected with Ti-major bottles (Figure 4b). At the southern end, an 8-m-high inactive chimney (from which sulfide sample D392-R8 was collected; Figures 4b and S2b) was perched at the top edge of a collapse in a lava flow. In 2012 and 2015, clear shimmering fluids were observed venting through cracks in the lava flow at the base of this chimney (Figure S2b).
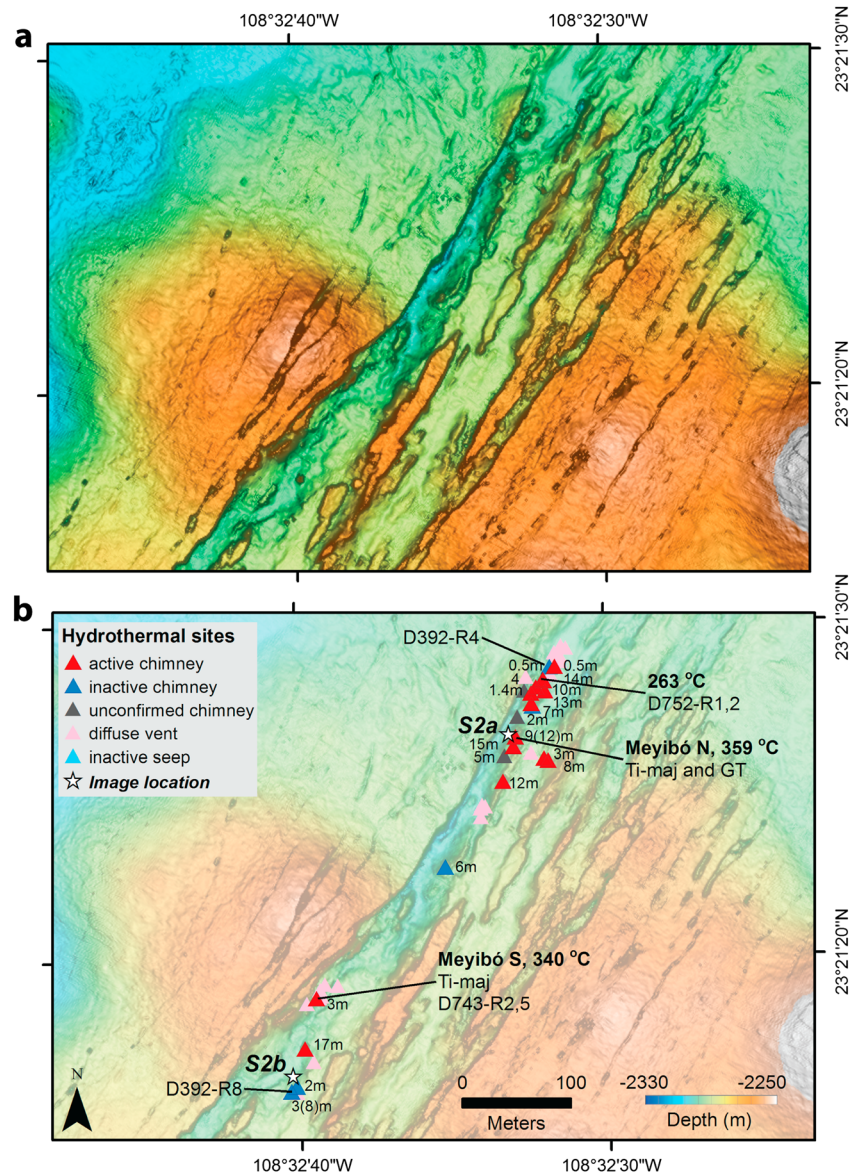
Figure 4. The Meyibó hydrothermal vent field on the Alarcón Rise. (a) AUV bathymetry map and (b) map with interpretations and data shown. The triangles indicate that activity of chimneys identified in the bathymetry and as classified from the ROV as active or inactive, and sites of diffuse venting observed from the ROV. Chimneys are labeled with the heights measured in the AUV data, and also in parentheses as determined from the ROV, if different. Also indicated are measured fluid temperatures and locations of analyzed deposit and fluid samples (Ti-maj, titanium major element; GT, gas-tight). Locations of images in Figures 6 and S2 are white stars labeled like *6a* and *S2a*. Location of map is shown in Figure 2.

Chimney fields Ja Sít and Pericú are located 1.7 km and 800 m northeast of the northern end of Meyibó, respectively, and are near the eruptive fissure producing the same young channelized basaltic lava flow (Figure 2; Clague et al., 2018). Ja Sít consists of two chimney clusters 250 m apart (Figure 5), 150 to 400 m west of the fissure, and along channels of the lava flow. One white-smoker chimney was 13 m high as measured by the ROV (see Text S1), and its temperature was 289 °C during dive D399. Clear fluids bathe tubeworm clumps growing midway up its spire and focused flow rises through the orifice of a narrow pipe that protrudes from the top of the chimney (Figure 6a). Two other chimneys at Ja Sít are over 10 m high. Diffuse flow also percolates through cracks in the lavas. Pericú is on the western edge of the eruptive fissure of the young channelized flow (Figures 7a and 7b). It was explored during dive D743 and has two vigorous black smoker chimneys 7 and 9 m high with many tall, slender orifices (Figure S2c).
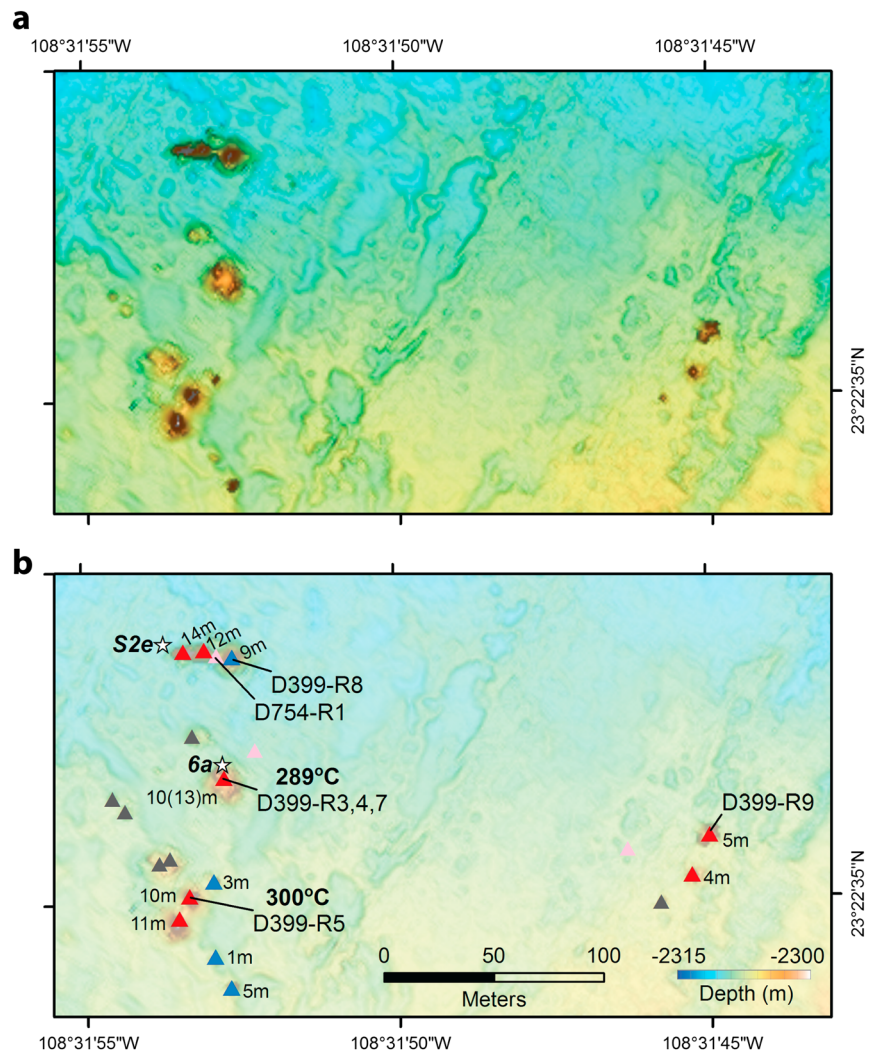
Figure 5. Ja Sít vent field (a) AUV map and (b) map with interpretations superimposed as in Figure 4. Location shown in Figure 2.

Between Pericú and Ja Sít and along the same fissure system is a small group of three chimneys up to 16 m high identified on the AUV maps. There was no temperature anomaly in the AUV CTD data near them; thus, they were not investigated by ROV and their status remains unknown (Figure 2).

The fourth active field on the Alarcón Rise, Tzab-ek (Figures 7c and 7d), is a tight cluster of eight chimneys that grew on an older hummocky flow on an upfaulted bench at the margin of the axial graben, above the young channelized flow and 850 m west of its eruptive fissure. The tallest chimneys on the Alarcón Rise are in this field and are black smokers 33 and 31 m high (AUV bathymetry had indicated the chimneys were 18 and 27 m high, respectively; see Text S1). The 33-m chimney was venting 330 ℃ fluids, and an 18-m-high black smoker was venting 355 ℃ fluids. A 20-m-high chimney was venting clear shimmering fluid. Several chimneys had sulfide flanges under which buoyant, hot fluids exit, pond, and water-fall upward, building the flanges outward as minerals precipitate from the fluid (Figure S2d). The chimneys rise from the center of an ~60-m diameter mound of massive sulfide and chimney talus that covers the underlying basalt and is at least 5 m thick (as determined from change in the ROV depth sensor).

Each active vent field on the Alarcón Rise has chimneys in various stages of development, with some chimneys that are waning in their activity or are inactive, sometimes next to active chimneys. Abundant *Riftia* worm tubes that were attached but empty and hanging (Figure S2e) indicate that a 14-m-high chimney in
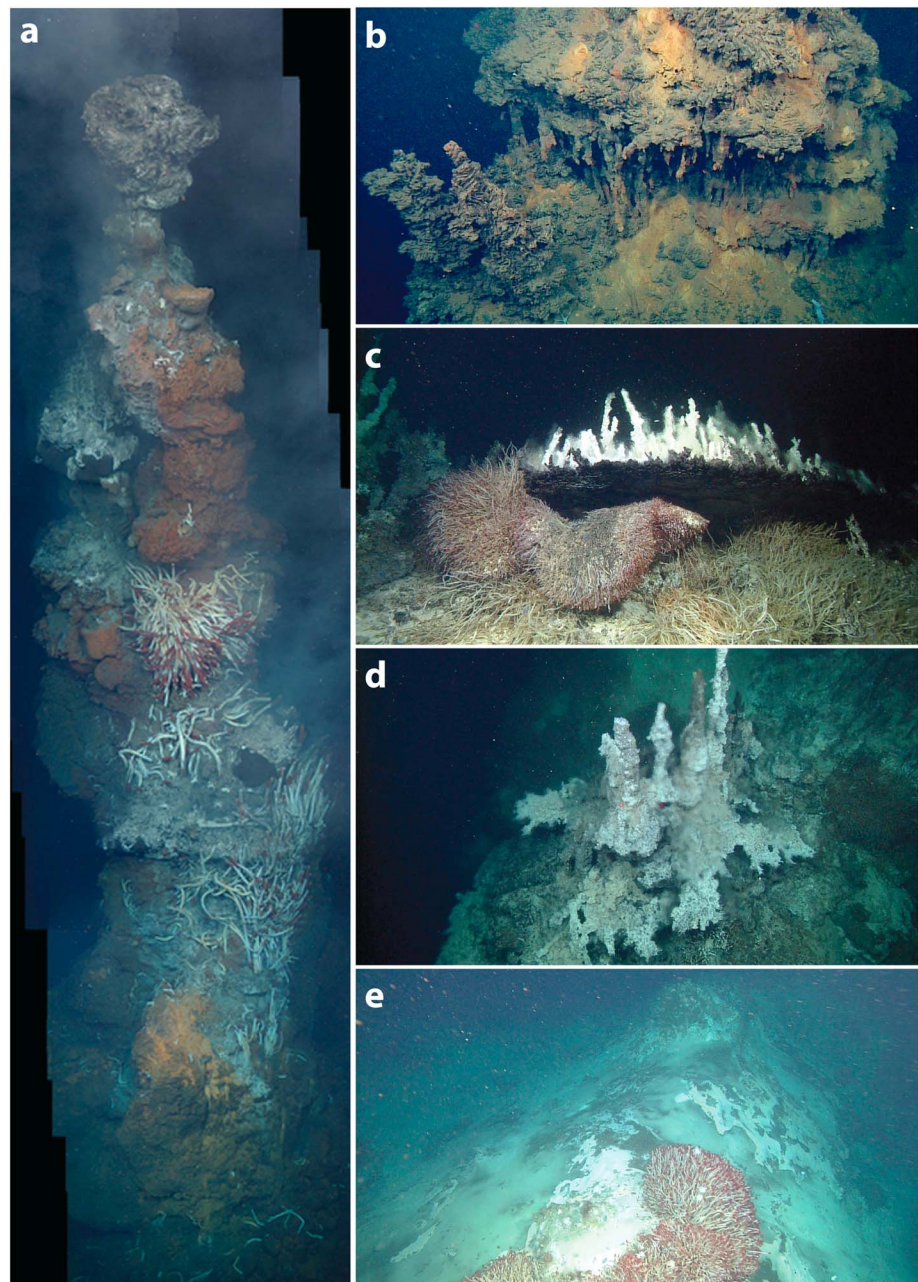
Figure 6. ROV video framegrabs of newly discovered hydrothermal sites. (a) Mosaic from framegrabs of the top approximately two thirds of the 13-m-high chimney in the Alarcón Rise Ja Sít field colonized by *Riftia pachyptila*. Location is white star on map in Figure 5. (b) The 10-m-high spire in the ICF, from which samples D395-R24 and D395-R25 were collected, has rusticles of oxidized metal-sulfide hanging from near the top of the edifice; location in Figure 8. (c) Clear fluids measuring 291 °C pond underneath a flange, waterfall upward, and deposit delicate spires at the top of the 27.5-m-high carbonate chimney in the Pescadero Basin. Dense colonies of *Oasisia* tubeworms are clustered below the flange. (d) Delicate fairy-castle spires and flanges on the 27.5-m-high chimney *P* in the Pescadero Basin. The red dots are lasers set 29 cm apart for scale. (e) Smooth mound ~4 m high in the Pescadero Basin is diffusely venting fluids that support thick bacterial mat and patches of tubeworms. Locations of c, d, and e are in Figure 9.

the Ja Sít field has recently become less active. Greatly reduced fluid flow through the edifice is indicated by the absence of vent-specific megafauna at some chimneys, but with sparse, light coatings of microbial mat. Farther away from the active chimneys and diffuse vents, the seawater is still milky and populations of mushroom sponges (*Caulophacus* sp.) and serpulid worms dot the pillow lavas. The carnivorous sponge
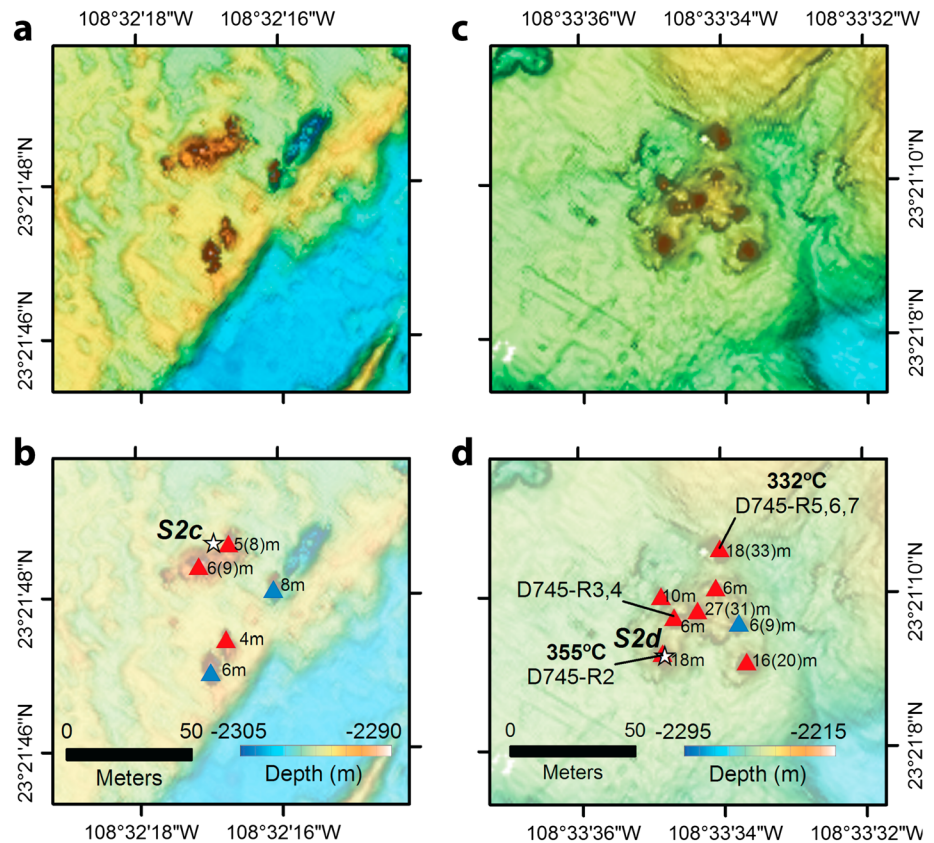
Figure 7. Alarcón Rise vent fields (a) Pericú AUV map and (b) map with interpretations as in Figure 4 and (c) Tzab-ek AUV map and (d) map with interpretations. Locations shown in Figure 2.

Cladorhiza evae (Lundsten et al., 2014) is abundant on surfaces of inactive chimneys and surrounding lava flows.

Forty-one inactive chimneys occur on the Alarcón Rise between 23°27′ and 23°28.3′N latitude, almost 10 km northeast from the nearest active field, Ja Sít (Figure 2). This field of inactive chimneys will henceforth be called the *ICF*. The chimneys are in two ridge-parallel, en echelon arrays stretching 2.6 km along axis (Figure 8). The southwest end of the western array is associated with several parallel fractures 50 to 100 m apart, and the eastern array is along fractures offset from the western array by ~500 m. The fractures cross moderately sediment-covered, channelized lava flows that are between about 270 and 1,000 years minimum age (Clague et al., 2018). The chimneys are almost 100 m deeper than the active fields (to 2,392-m depth). The western array extends northeast to 2,330-m depth on the flank of a broad lava shield with a 30-m-deep summit crater that dates to ~320 ± 30 year minimum age (Clague et al., 2018).

Despite being oxidized, many of the inactive chimneys remain quite tall: six were between 10 and 15 m high. One had long drips of secondary iron oxyhydroxide hanging from the edifice, which we called rusticles because they are reminiscent of the way iron rusts on shipwrecks (Figure 6b). Nonchemosynthetic deep-sea animals, such as soft corals, hydroids, and sponges, were abundant near the tops of the inactive chimneys (Figure S2f).

Partially dissolved vesicomyid clam shells were observed in two sites that were not associated with active venting or chimneys, so are considered inactive seep sites. One was about 1.5 km north of Ja Sít at 108°28.5′W, 23°23.2′N (Figure 2), in a tectonically faulted region where there were no chimneys or signs of currently active fluid flow, and the other was on the broad lava shield at 108°28.8′W, 23°27.7′N, near inactive chimneys in the ICF (Figure 8b).
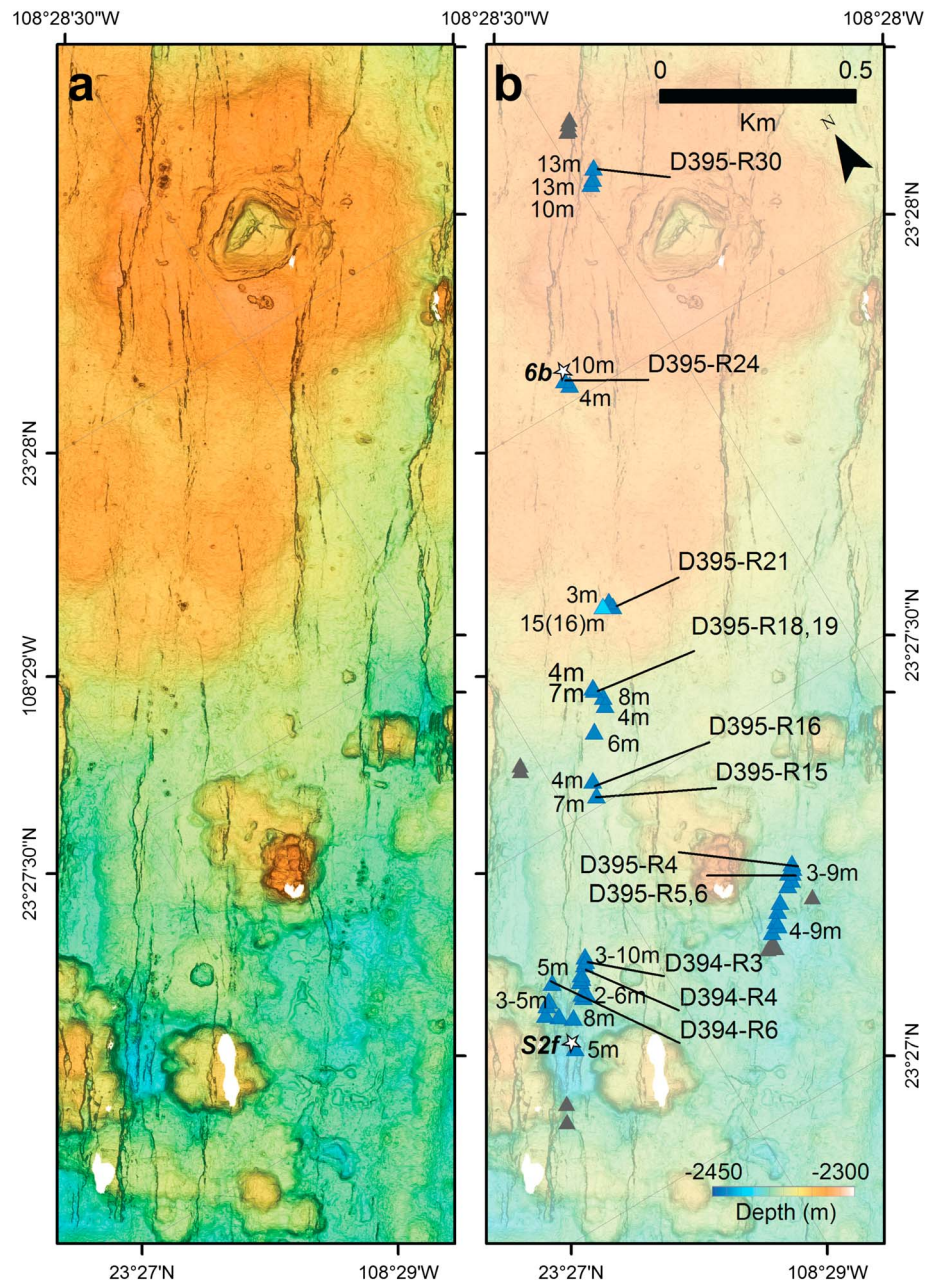
Figure 8. Chimneys referred to in the text as the "inactive chimney field" (ICF) between latitudes of 23°27' and 23°28.3'N (a) AUV map and (b) map with interpretations as in Figures 2 and 4. Location shown in Figure 2.

3.2.2. Pescadero Basin Hydrothermal Field

AUV mapping of the Auka hydrothermal field in the southern Pescadero Basin revealed several large mounds and numerous smaller mounds that rise above the otherwise smooth sediment-covered bottom in the southwest corner of the basin (Figure 3a). The three largest mounds are actively venting, steep-sided edifices 12–25 m high, with base diameters of 15–50 m (Figure 9), that we called the C, P, and Z chimneys. They have well-developed flange structures topped by abundant, delicate, white spires (Figures 6c and 6d) mainly constructed of calcite. Clear vent fluids, up to 291 °C, pond in reflective pools under the flanges and spill upwards (Figure 6c). Thick microbial mats and dense, *Oasisia* tubeworm clusters are bathed by lower temperature fluids escaping through the sides of the chimneys (Figure 6c; Goffredi et al., 2017). The broad mounds consist of accumulated chimney and flange talus.
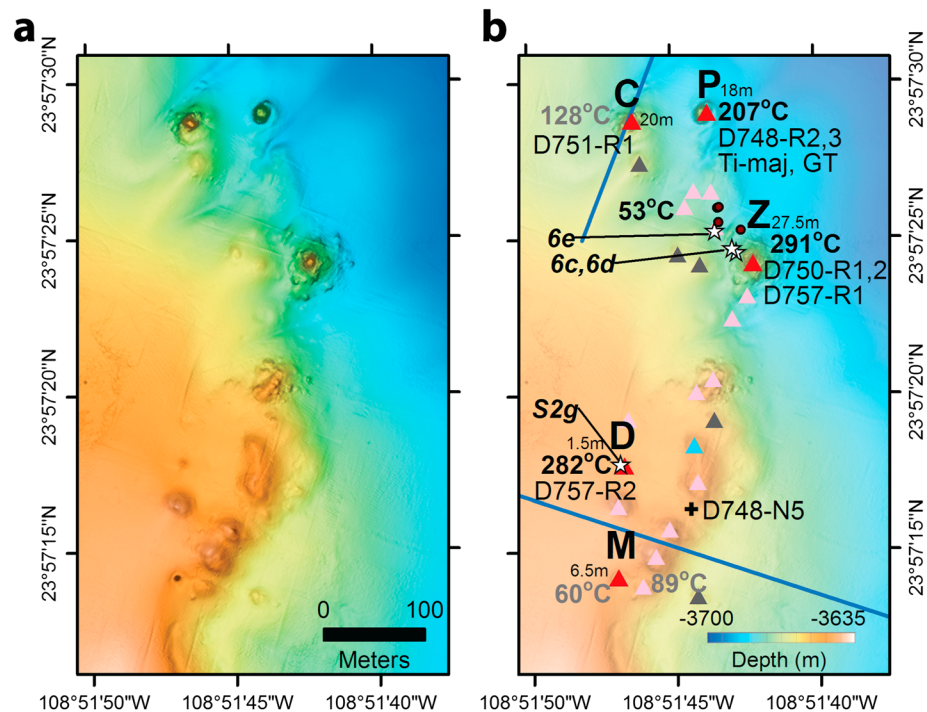
Figure 9. Auka active hydrothermal field in southern Pescadero Basin (a) AUV map and (b) map with interpretations as in Figure 4. Largest chimneys are *C*, *P*, and *Z*, and smaller ones are *D* for Dianne's vent and *M* for Matterhorn. Sediment push core locations are brown dots. Temperatures taken of fluids bathing animals rather than the hottest effluent are in gray. D748-N5 is one of the background water samples in Table 1 (see Text S2). The blue lines are tracks of subbottom profiles in Figure 3. Location shown in Figure 3a.

A fourth, high-temperature vent (≥282 °C) named Dianne's Vent has a 75-cm-wide orifice confined by 10-cm-wide chimney walls that only rise about 1.5 m above a small carbonate mound composed of chimney and flange talus, and a fifth chimney, named Matterhorn, is a narrow, tapered hydrothermally active spire, 6.5 m high (Figure 9b). These vents were first observed during the biology dive leg, when fluid samplers were no longer on the ship.

The areas between the large chimneys and extending to the south, aligned parallel with the fault scarp, are broad, low, and smooth mounds (Figure 6e), some of which are diffusely venting clear fluids and sheathed with thick white microbial mat. Clams and clumps of tubeworms also grow on some mounds (Goffredi et al., 2017). The bases of the mounds typically transition over tens of meters from hydrothermal carbonate crust in sediment to microbial mat covered sediment to communities of vesicomyid clams and outward to dense colonies of zoanthids where hard carbonate crusts are present, passing into hemipelagic sediment with sparse vesicomyid clams and burrowing anemones.

3.3. Chemical Composition of Hydrothermal Fluid Samples

Selected elements from analyses of the fluids recovered with Ti-major samplers are presented as end-member hydrothermal fluids in Table 1, after extrapolation to 0 mmol Mg/kg to correct for seawater contamination as calculated in supporting information Table S1. Dissolved gas compositions of fluids collected with gas-tight bottles are in Table 2.

3.3.1. Alarcón Vent Fluids

Hydrothermal fluids were collected in 2015 from two vigorous black smoker vents in the Meyibó field on dive D743 (Figure 4b). The vent sampled at the northern end of the field, Meyibó N, had a temperature of 359 °C, and Ti-major (Figure S2a) and gas-tight bottles collected fluids. The vent sampled at the southern end of the field, Meyibó S, had a temperature of 340 °C, and fluids were collected with Ti-major bottles only. The chlorinity of Meyibó N is 571 mmol/kg (6% higher than the 538 mmol/kg measured for bottom seawater, collected with Niskin bottles on the ROV); however, Meyibó S is only slightly higher in chloride than seawater

Table 1
Bottom SW and Ti-Major Endmember Values Extrapolated to 0 mmol Mg/kg

Parameter	Units	Bottom water	Auka P	Meyibó S	Meyibó N
Dive			D748	D743	D743
# of samples			3	2	2
Latitude		[a]	23.96	23.36	23.36
Longitude		[a]	−108.86	−108.54	−108.54
Depth	m	[a]	−3673	−2291	−2286
Temperature	°C	2	207 (291)	340	359
pH (at 25° C)			6.3	3.4	3.3
Mg[b]	mmol/kg	53	9.1	1.2	3.0
			Endmember	Endmember	Endmember
Ca	mmol/kg	10.3	42.4	21.2	19.4
Sr	µmol/kg	90.0	273	109	107
Sulfate	mmol/kg	28.0	2.0	5.9	6.6
Na	mmol/kg	466	523	482	520
K	mmol/kg	10.1	46.1	30.1	31.2
Li	µmol/kg	26.6	1750	825	870
B	µmol/kg	410	1525	343	350
Mn	µmol/kg	0	115	630	945
Fe	µmol/kg	0	25.6	1451	4300
Ba	µmol/kg	0.15	54.9	44.3	38.6
Si	mmol/kg	0.18	11.6	18.7	16.1
Sulfide (Zn)	mmol/kg	0	10.6	5.6	6.2
Chlorinity	mmol/kg	538	646	541	571
V	nmol/kg	37.4	0	21	23
Cr	nmol/kg	6.9	24	22	52
Co	nmol/kg	0.1	1	86	70
Ni	nmol/kg	11	49	72	190
Cu	nmol/kg	10	37	51	97
Zn	nmol/kg	10	4500	1000	4500
Rb	µmol/kg	1.43	87	18	17
Y	nmol/kg	0.33		0.4	0.3
Mo	nmol/kg	112	0	0	0
Cd	nmol/kg	2.3	0.8	0.2	0
Cs	nmol/kg	2.4	11000	860	850
U	nmol/kg	12.8	0	0	0
$\delta^{18}O$	‰ VSMOW	−0.93[c]	1.49	0.71	0.88
δD	‰ VSMOW	−1.1[c]	3.7	−0.7	−1

Note. Locations of Niskin bottom seawater samples are in supporting information Text S1. Complete analyses are in supporting information Table S1. VSMOW = Vienna standard mean ocean water.
[a]Bottom water was an average of D740-N5 and D748-N5.   [b]Lowest measured Mg value.   [c]Bottom water isotope values from Niskin sample D747-N5.

(Figure 10a). The 359 °C Meyibó N vent fluid has significantly higher concentrations of Fe, Mn, Cu, and Zn but has somewhat lower Si content, compared to the 340 °C vent fluid (Table 1). Both have acidic fluids, with $pH_{25\,°C}$ averaging 3.3 (Table 1 and Figure 10b). The $\delta^{18}O$ values are 0.88‰ and 0.71‰ Vienna standard mean ocean water (VSMOW) for Meyibó N and Meyibó S vent fluids, respectively, and δD values are −1‰ and −0.7‰ VSMOW (Table 1). Bottom seawater collected at a similar depth has a $\delta^{18}O$ value of −0.93‰ VSMOW and δD of −1.1‰ VSMOW (Table 1). The Meyibó N vent fluid has high CO_2 and CH_4 contents (28.6 and 2.7 mmol/kg, respectively; Table 2). Helium is 2,472 nmol/kg, $^3He/^4He$ is 8.21 R_a, and higher hydrocarbons are all below 0.3 µmol/kg (Table 2).

3.3.2. Southern Pescadero Basin Vent Fluids

A single vent in the Auka vent field was sampled for hydrothermal fluids during the weather-shortened dive D748. Three Ti-major element samples and three gas-tight samples were collected from the same vent orifice (Figure 9b). Thin carbonate spires that topped chimneys (e.g., Figures 6c and 6d) lacked good orifices, which made temperature measurements unreliable and resulted in seawater entrainment in the sampled fluids. The lowest Mg contents were 9.0 and 9.7 mmol/kg Mg for the major element and gas tight samples, respectively (Table 1), indicating ~20% seawater dilution. The maximum temperature reading in the vent orifice was

Table 2
Data from Gas-tight Fluid Samplers

Parameter	Units	Auka P	Meyibó N
Dive		D748	D743
# of samples		3	2
Latitude		23.96	23.36
Longitude		−108.86	−108.54
Mg^a	mmol/kg	9.7	4.0
		Endmember	Endmember
He	nmol/kg	824.5	2472
$^3He/^4He$	Ra	7.7	8.2
H_2	mmol/kg	2	0.5
N_2	mmol/kg	**1.18**	0.67
Ar	mmol/kg	**0.02**	0.02
CH_4	mmol/kg	81	2.7
CO_2	mmol/kg	49.2	28.6
C_2H_4	μmol/kg	1.2	0.18
C_2H_6	μmol/kg	2300	0.24
C_3H_4	μmol/kg	0.3	0.03
$C_3H_6 + C_3H_8$	μmol/kg	680	0
C_4H_{10}	μmol/kg	113	**0**
$isoC_4H_{10}$	μmol/kg	73	**0**
$CH_4/C_2 + C_3 + C_4$		26	**5895**

Note. Endmember values extrapolated to 0 mmol Mg/kg to correct for seawater dilution, except for those in bold, for which the reported value is the value measured in the sample with the lowest Mg concentration. CO and C_2H_2 were below detection.
aLowest measured Mg value.

207 °C, but the measured temperature was likely lower than the true temperature due to entrainment of seawater. We infer that the temperature of the end-member fluid is likely to be closer to 290 °C, as measured in pools underneath flanges of a nearby chimney, where stable vent temperature could be obtained.

Auka vent fluids have elevated chlorinity at 646 mmol/kg, ~20% higher than seawater (Table 1 and Figure 10a); have nearly neutral $pH_{25\ °C}$ of 6.3; and are enriched in highly soluble elements such as B and alkalis (Figures 10b and 10c), with high Li, Rb, and Cs contents (Figure 10d and Table 1). Trace metal contents of Fe, Mn, and Cu are lower than those in the Alarcón Rise vent fluids, but Zn concentration (4,500 nmol/kg) is as high as from one chimney at Alarcón Rise (Table 1).

Auka vent fluids have elevated values of $\delta^{18}O$, at 1.49‰ VSMOW, and δD, at 3.7‰ VSMOW (Table 1). The fluids have high concentrations of dissolved gas (Table 2), with highly elevated concentrations of CO_2, CH_4 (Figure 10e), and higher order hydrocarbons but lower ratios of CH_4 relative to higher order hydrocarbons than at Alarcón Rise. Helium concentration is low, at 824.5 nmol/kg, but the He isotope ratio is only slightly lower than the Alarcón Rise vent, at 7.67 R_a (Table 2).

### 3.4. Mineralogy and Chemistry of Hydrothermal Deposits

Samples were broken from chimneys, including pieces of active conduit, or collected from talus at the base (see Table 3), and representative bulk subsamples analyzed. Selected elements from analyses of the samples are presented in Table 3, and the complete data set and quality control information are in Table S2.

3.4.1. Hydrothermal Samples From Alarcón Rise Vent Fields

Samples were collected from three of the active vent fields: from four chimneys at Meyibó (Figure 4b), four at Ja Sít (Figure 5b), and three at Tzab-ek (Figure 7d); some were from chimneys that are no longer active (Table 3 and Figures 4b and 5b). Samples were also collected from 11 chimneys in the ICF (Figure 8b).

Sulfur content of the samples ranges from 19 to 52 wt% (Table 3), and the mineralogy includes variable proportions of pyrrhotite, pyrite, marcasite, sphalerite, chalcopyrite, isocubanite, and anhydrite as the dominant mineral phases. Some samples have minor amounts of barite. Active chimney conduits are typically lined with coarse bladed intergrown isocubanite-chalcopyrite (e.g., Figure 11a; D743-R2). At least one chimney sample from Ja Sít (D399-R5) and one from Meyibó field (D752-R1A) contain abundant bornite. Sample D752-R1A is zoned (chimney interior to exterior) from intergrown isocubanite-chalcopyrite –> chalcopyrite –> bornite –> covellite. Samples from the more mature inner portions of chimneys are often composed of more homogeneous chalcopyrite with large (1–2 mm) euhedral pyrite porphyroblasts (e.g., D395-R30; Figure 11b). In some, fossilized remains of tubeworm tubes were infilled with sulfide (Figure 11c), as described by Cook and Stakes (1995).

The sulfide samples from Alarcon Rise are similar in most respects to other mid-ocean ridge hydrothermal deposits. There is likely a sampling bias in that chimney tops, active or inactive, are easier to sample compared to chimney interior or mound samples, which likely biases the sample suite to higher base and precious metal grades due to zone-refining and remobilization of metals (Hannington et al., 1995; Humphris et al., 1995; Monecke et al., 2016), but they compare well with other mid-ocean ridge deposits (e.g., Hannington et al., 2005). Average grades for the sample suite are slightly over 6 wt% Cu and 6 wt% Zn, but the samples tend to be either high Cu or high Zn (Table 3 and Figure 12). There is a tendency for the inactive chimney samples to show higher Zn contents, which likely reflect later-stage, lower temperature venting in the inactive vent fields as thermal activity wanes (Hannington et al., 2005). The Zn-rich samples have the highest precious metal contents (up to 1.95 ppm Au and 872 ppm Ag), which are strongly correlated with each other and with Sb (Figures S3a and S3b). Enrichment of Ag, Au, Cd, Ga, Ge, and Sb (Figures 12d and S3c) is typical of lower temperature, zinc-rich deposits worldwide (Hannington et al., 2005; Monecke et al.,
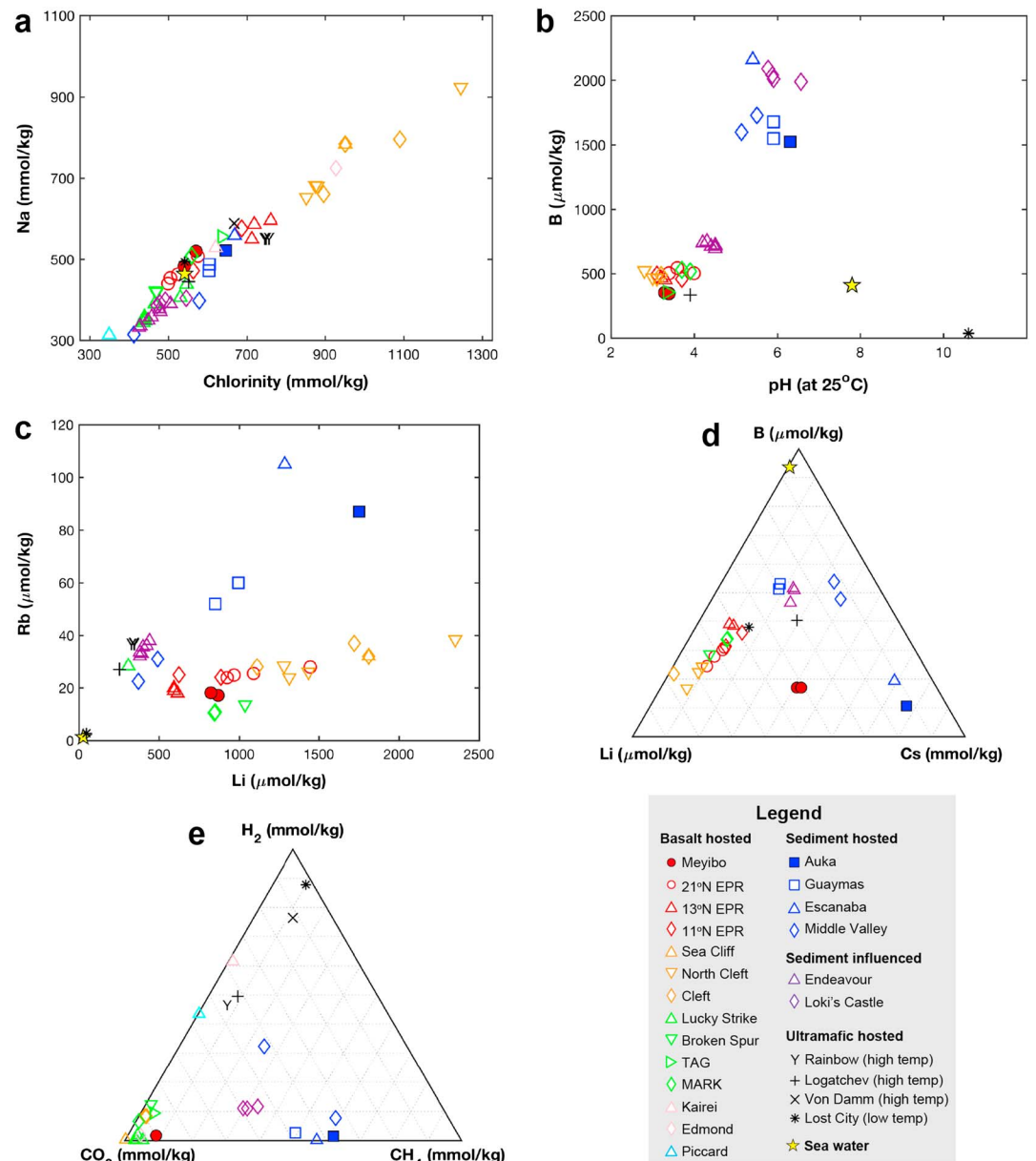
Figure 10. Geochemistry of Meyibó (Alarcón Rise) and Auka (Pescadero Basin) hydrothermal fluids compared with fluids from different environments. Most data are from the IEDA EarthChem VentDB chemistry data collection (Mottl, 2012; see text for references) and exclude low-salinity vents. (a) Plot of chlorinity versus Na. (b) Plot of pH measured at 25 °C verses B. Sediment-influenced systems show elevated B and nearly neutral pH. (c) Plot of Rb versus Li. Sediment-hosted systems tend to have high concentrations of highly soluble elements, including alkali elements, but the concentrations are also influenced by the salinity of the vent fluid. Sediment-influenced systems form a distinctive array with higher Rb/Li compared to systems hosted by mafic and ultramafic rocks. (d) Relative concentrations of Li, B, and Cs. Auka fluids are most similar to those from Escanaba Trough. (e) Plot of the relative abundances of CO_2, H_2, and CH_4 for representative vent fluids. Basalt-hosted, sediment-hosted, and ultramafic hosted systems generally plot in different parts of the diagram.

2016). Copper-rich samples have elevated Se and In, similar to other mid-ocean ridge sulfide samples (Monecke et al., 2016).

3.4.2. Hydrothermal Samples From Pescadero Basin

Samples were collected from four chimney structures at the Auka vent field (Figure 9b). Here the high-temperature hydrothermal fluids precipitate nearly pure calcite and form delicate white chimneys and flanges (Figure 11d) on the massive mounds (Figure 9b). The diffusely venting mounds also are

Table 3
*Partial Chemical Analyses of Bulk Hydrothermal Samples*

Sample	Latitude	Longitude	Depth	Field	Activity	Sample type	Total S (%)	Zn (ppm)	Cu (ppm)	Fe (%)	Si (%)	Mg (%)	Ca (%)	Au (ppb)	Ag (ppm)	Ba (ppm)	Cd (ppm)	Pb (ppm)	Se (ppm)	Sr (ppm)
Method							IR/CS	ICP	ICP	ICP	ICP	ICP	ICP	INAA	INAA	ICP	ICP	ICP	ICP	ICP
Detection limit							0.0	30	2	0.1	0.01	0.01	0.01	2	5	3	2	0.8	0.8	3
Alarcón Rise																				
D745-R3	23.35259	−108.55965	2236	Tzab-ek	Active	Chimney	38.1	78,800	182,000	31.6	0.30		0.03	59	59	31	338	78	247	17
D745-R4	23.35267	−108.55980	2253	Tzab-ek	Active	Talus	44.1	2,180	119,000	37.9	0.69	0.02	0.05	14		36	10	43.6	84.1	19
D745-R7	23.35286	−108.55945	2252	Tzab-ek	Active	Talus	45.1	46,900	13,800	34.6	0.20	0.01	0.09	46		13	168	485	94.7	19
D745-R6	23.35287	−108.55942	2252	Tzab-ek	Active	Talus	47.2	760	56,500	41.2	0.93	0.53	0.02			6	3	83.6	363	26
D745-R5	23.35288	−108.55943	2252	Tzab-ek	Active	Talus	45.1	72,600	66,500	33.3	0.18	0.03	0.08	105	59	473	223	784	157	52
D392-R8	23.35456	−108.54442	2287	Meyibó	Not venting	Chimney	32.7	241,000	4,320	14.9	3.82			862	872	23	772	19,300	14.2	53
D743-R2	23.35525	−108.54431	2291	Meyibó	Active	Clogged conduit	38.1	10,200	185,000	38.0	1.00	0.01	0.08	39	41	2,570	29	301	156	131
D743-R5	23.35525	−108.54431	2291	Meyibó	Active	Chimney	22.5	1,570	9,730	3.4	1.59	0.50	25.5			225	9	27.9	4.0	2,560
D752-R1A	23.35793	−108.54218	2299	Meyibó	Not venting	Talus	33.2	280	330,000	29.9	0.21	0.12	0.16			14	3	7.3	2,240	18
D752-R1B?	23.35793	−108.54218	2299	Meyibó	Not venting	Talus	43.1	218,000	27,600	30.1	0.15	0.03	0.03	48		10	918	299	117	20
D752-R2	23.35793	−108.54220	2299	Meyibó	Not venting	Talus	48.3	2,060	764	40.4	0.93	0.03	0.04			3,830	5	397	2.3	568
D392-R4	23.35806	−108.54205	2298	Meyibó	Not venting	Talus	46.5	1,650	31	38.1	3.63					4,180	3	585	3.3	150
D399-R3A	23.37702	−108.53130	2289	Ja Sit	Active	Conduit	51.1	10,800	982	44.1	0.72			28	< 5	1,460	13	1,050	5.6	47
D399-R3B	23.37702	−108.53130	2289	Ja Sit	Active	Conduit	35.7	4,600	110,000	33.7	0.03	0.02	6.37		25	879	17	105	205	623
D399-R5	23.37646	−108.53147	2302	Ja Sit	Active	Conduit	29.9	2,730	148,000	19.5	0.20	0.22	12.2		15	23	13	13.3	277	1,290
D399-R9	23.37679	−108.52910	2304	Ja Sit	Active	Talus	37.3	35,500	11,500	50.8							158	90.5	109	
D399-R4	23.37706	−108.53120	2304	Ja Sit	Active	Talus	45.3	4,730	79,800	42.0			0.04	81	29		27	61.6	104	
D399-R7	23.37706	−108.53130	2304	Ja Sit	Active	Talus	51.6	800	10,900	46.3								128	19.0	
D754-R1	23.37746	−108.53132	2308	Ja Sit	Active	Talus*	45.8	84,900	1,290	37.6	0.16	0.02	0.06	360	127	3,320	157	1,100	290	185
D399-R8A	23.37752	−108.53125	2298	Ja Sit	Not venting	Talus	38.6	1,880	193,000	37.9				45	26	90	8	71.1		
D399-R8B	23.37752	−108.53125	2298	Ja Sit	Not venting	Talus	46.2	7,710	17,500	41.7				77	32	11	21	79.6	146	
D395-R5	23.45464	−108.47932	2382	ICF	Not venting	Talus	51.7	6,170	6,290	44.4	0.18	0.03		23			20	77.2	29.8	
D395-R6	23.45464	−108.47932	2382	ICF	Not venting	Talus	28.3	86,300	3,600	21.6	17.20		0.03	356	184	230	258	808	4.7	245
D395-R4	23.45477	−108.47920	2385	ICF	Not venting	Conduit	19.1	96,000	1,120	13.6	23.50			1,040	226	3,820	176	7,360	4.2	
D394-R4	23.45530	−108.48514	2370	ICF	Not venting	Talus	30.3	373,000	2,650	7.5	6.14			808	251	483	1,640	2,380	14.9	
D394-R3	23.45546	−108.48490	2380	ICF	Not venting	Conduit talus	47.3	6,940	21,000	40.0	0.13	0.03		66		39	59	142	3.4	
D394-R6	23.45547	−108.48595	2378	ICF	Not venting	Talus	43.7	1,330	41,700	37.5	0.05		0.18				23	142	64.5	
D395-R15	23.45856	−108.48258	2369	ICF	Not venting	Conduit	44.8	2,290	71,300	43.8	0.31			31	26	3,720	11	48.1	21.3	339
D395-R16	23.45880	−108.48250	2374	ICF	Not venting	Talus	32.6	371,000	3,840	13.0	1.62			765	205	113	1,520	2,460	15.8	

Table 3 *(continued)*

Sample	Latitude	Longitude	Depth	Field	Activity	Sample type	Total S (%)	Zn (ppm)	Cu (ppm)	Fe (%)	Si (%)	Mg (%)	Ca (%)	Au (ppb)	Ag (ppm)	Ba (ppm)	Cd (ppm)	Pb (ppm)	Se (ppm)	Sr (ppm)
Method							IR/CS	ICP	ICP	ICP	ICP	ICP	ICP	INAA	INAA	ICP	ICP	ICP	ICP	ICP
Detection limit							0.0	30	2	0.1	0.01	0.01	0.01	2	5	3	2	0.8	0.8	3
D395-R19	23.46072	−108.48123	2357	ICF	Not venting	Talus	34.1	409,000	4,380	10.4	0.08			1,950	369	66	1,760	894	17.2	
D395-R18	23.46074	−108.48120	2358	ICF	Not venting	Talus	36.1	960	76,300	32.8	6.24	0.02					2	272	111	682
D395-R21	23.46211	−108.47979	2332	ICF	Not venting	Chimney	35.5	270,000	5,560	17.9	4.14			1180	319	80	1,480	1,080	11.8	
D395-R24	23.46738	−108.47765	2343	ICF	Not venting	Talus	45.8	133,000	5,290	31.1				279	32	51	690	1,380	11.8	
D395-R30	23.47099	−108.47447	2316	ICF	Not venting	Chimney	34.6	590	266,000	31.9	0.05	0.06			22		2	9.6	155	
Pescadero Basin																				
D757-R2	23.95491	−108.86299	3651	Auka	Active	Conduit	13.1	550	4,830	0.6	5.01	3.63	24.8	29	31	3,810	5	13,100	167	1,810
D757-R1	23.95673	−108.86180	3659	Auka	Active	Flange	0.8	920	417	0.4	0.47	0.20	38.1	48		620	9	808	6.1	913
D750-R2	23.95676	−108.86180	3666	Auka	Active	Flange	2.4	1,760	855	0.7	4.72	0.50	33.0	134	35	7,110	12	1,210	17.1	996
D751-R1	23.95783	−108.86292	3664	Auka	Not venting	Flange	0.7	2,330	835	0.5	0.26	0.04	38.3	20	15	566	18	1,150	6.2	702
D748-R3B	23.95811	−108.86228	3670	Auka	Active	Conduit	0.8	1,100	549	0.6	0.54	0.17	37.7	78	16	344	8	761		618
D748-R2	23.95813	−108.86223	3673	Auka	Active	Flange	1.2	970	766	1.0	10.70	0.09	28.2	208	38	2,400	6	713		518

Note. Complete analyses in supporting information Table S2;. Analyses left blank were below detection; ICF = inactive chimney field between 23°27′ and 23°28.5′N latitude; *D754-R1 lay where fluids were diffusely venting between active and inactive chimneys.
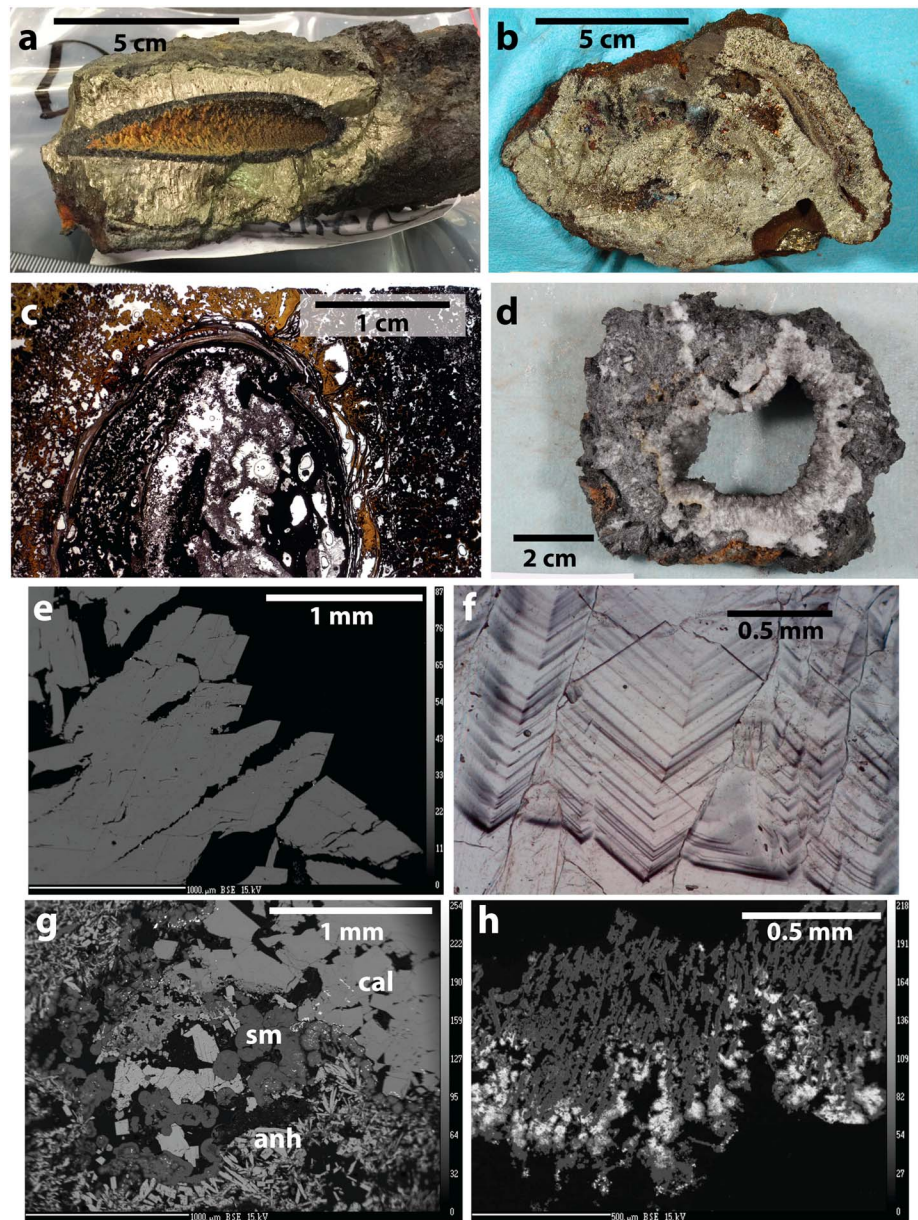
Figure 11. Samples from the hydrothermal chimneys. Collection locations are in Figures 4, 8, and 9. (a) Clogged orifice composed of chalcopyrite broken from a 3-m-high 340 °C active black smoker in the Meyibó field, sample D743-R2. It has an inner lining of bladed pyrrhotite (dark) and late stage overgrowth of barite stained orange by iron oxyhydroxide. (b) Isocubanite (copper-iron-sulfide) specimen broken from a 13-m-high inactive chimney in the ICF; D395-R30 (saw-cut surface). (c) Thin section cut through a fossilized cast of a tubeworm tube broken from an inactive sulfide chimney; D394-R4. (d) Cross section of a calcite-lined, actively venting orifice (D748-R3) from the 18-m-tall chimney *P* in the Auka field. (e) Backscattered electron (BSE) image of coarse bladed calcite in D748-R3, growth direction toward the upper right. (f) Photomicrograph showing growth zoning within calcite in D750-R2 in the Auka field. Growth direction is toward the bottom of the slide. Darker zones are defined by inclusions of sulfide minerals, dominantly pyrrhotite with chalcopyrite/isocubanite, galena, and sphalerite. (g) BSE image of D748-R3. A zone of coarse calcite (labeled *cal*, upper right) from the interior of the orifice and a zone of bladed anhydrite (*anh*, upper left and lower right) from the exterior of the spire have a transition zone between them (center). The transition zone includes blocky anhydrite (bright with cleavage traces), botryoidal aggregates of Mg-rich clay interpreted to be smectite (*sm*), and fine-gained calcite intergrown with clay. Sulfides and barite (bright) are concentrated in the transition zone. (h) BSE image of D748-R2 in the Auka field, showing amorphous silica (smooth, gray) overgrowing Mg-rich clay (darker gray) replacing anhydrite in the transition zone. Dominant sulfide is bladed pyrrhotite (bright) with less abundant base metal sulfides.
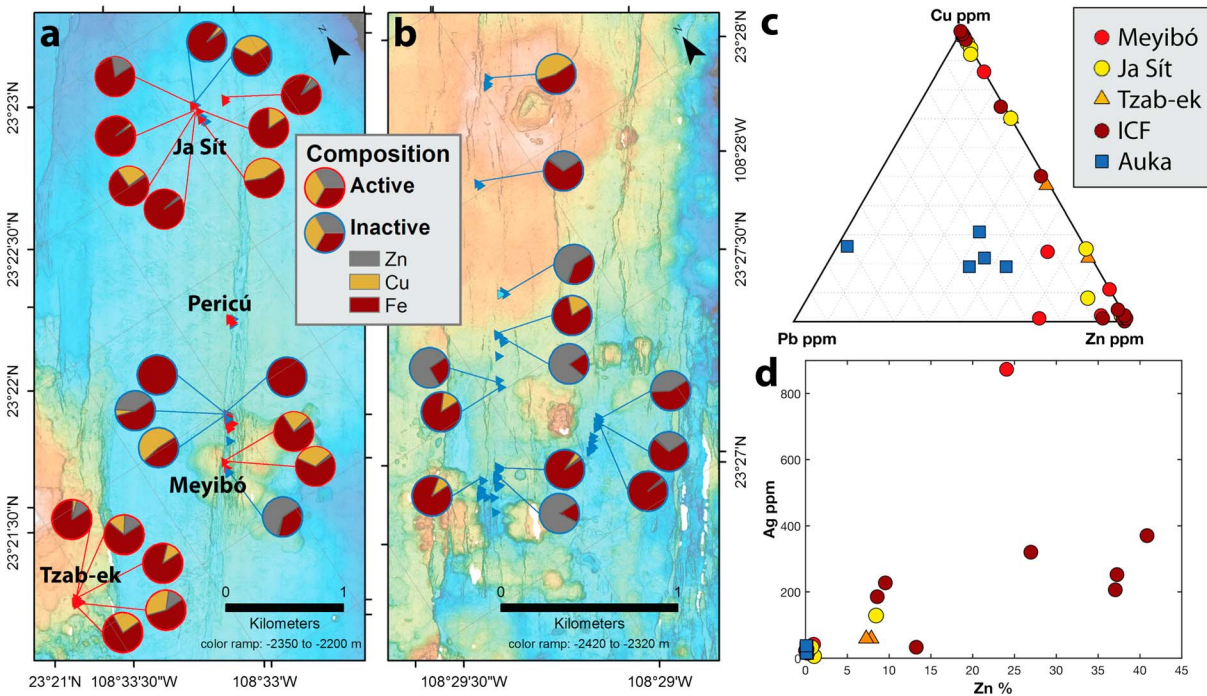
Figure 12. Geochemistry of hydrothermal deposits. (a) Map with pie diagrams showing relative composition of Zn, Cu, and Fe in deposits from the active fields and (b) from the inactive field on the Alarcón Rise. Samples are distinguished as having come from active chimneys by red color and from inactive chimneys by blue color of pie outlines and leaders setting pies off from collection locations, which are symbolized by triangles as in Figure 4. (c) Relative concentrations of Pb, Zn, and Cu and (d) plot of Ag versus Zn from chimneys from the Alarcón Rise Meyibó, Ja Sit, Tzab-ek, and ICF fields and from the Pescadero Basin from the Auka field. Symbols specify the hydrothermal field from which samples were collected, where ICF is the inactive chimney field between 23°27′ and 23°28.5′N latitude.

constructed almost entirely of calcite and calcite talus. On recovery, the samples had a faint odor of hydrocarbon.

The inner lining of chimneys (Figures 11d and S2g) and underside of flanges consist of large, blocky to elongate crystals of nearly pure calcite with elongated habits indicating unidirectional growth into the hydrothermal fluid (Figure 11e). Growth zones are highlighted by increased, but minor, amounts of sulfide minerals (Figure 11f). There is often a faint brownish stain, likely of hydrocarbon, along grain boundaries. The outermost portions of chimneys and the top of flanges exposed to seawater are composed of bladed anhydrite intergrown with increasing amounts of fine-grained calcite, and less abundant barite, closer toward the hydrothermal fluid. A transition zone typically separates the inner calcite lining and the outer anhydrite zone (Figure 11g). The dominant phase in the transition zone is clay with high-Mg and low-Al content with the optical properties of saponite. Sulfide minerals (Figure 11h) and bladed barite crystals are most abundant in the inner portion of the transition zone and decrease in abundance outward. Talus samples exposed to cold seawater show signs of calcite dissolution.

Total sulfur contents for most Auka samples were less than 2.5 wt% (Table 3), which includes sulfide and sulfate as anhydrite and minor barite. No massive sulfide talus or iron oxide gossans were observed in this vent field. With the exception of sample D757-R2, samples contain only trace amounts of sulfide. Pyrrhotite is the dominant sulfide and often occurs as fine-grained (<1 mm) crystals with plate-like morphology (Figure 11h). Pyrite was only observed in one sample, D748-R2 from chimney P, in trace amounts. Pyrrhotite is overgrown by subequal amounts of 1- to 20-μm crystals of intergrown chalcopyrite-isocubanite and sphalerite, with less common galena. The exception was D757-R2, broken from the orifice of the short, 282 °C, vigorous Dianne's Vent (Figures 9b and S2g), which has a S content of 13.1 wt% (Table 3). The interior wall fragment is coarsely crystalline, clear euhedral calcite crystals, on which a thin layer of amorphous silica intergrown with 1- to 2-mm euhedral crystals of galena was deposited, and lined with a millimeter-thick monomineralic band of chalcopyrite (Figure S2h).

Table 4

C and O Isotope Ratios for Pescadero Basin Calcite

Sample	Chimney	$\delta^{13}C$ (‰ VPDB)	$\delta^{18}O$ (‰ VSMOW)	T (°C)[a]	$\delta^{13}C_{CO2}$
D748-R2		−10.16	8.01		
D748-R2.1		−9.60	9.24		
D748-R2.2		−9.91	8.60		
D748-R2.3		−10.00	8.47		
D748-R2 *ave*	P	−9.92	8.58	256	−8.58
D748-R3B.1		−10.64	7.30		
D748-R3B.2		−10.62	7.33		
D748-R3B.4		−10.50	7.53		
D748-R3B *ave*	P	−10.58	7.38	290	−8.87
D750-R1.1		−10.63	7.09		
D750-R1.2		−10.71	6.93		
D750-R1.3		−10.70	6.87		
D750-R1 *ave*	Z	−10.68	6.96	304	−8.84
D750-R2.1		−11.01	7.00		
D750-R2.2		−11.06	6.63		
D750-R2.3		−10.88	6.89		
D750-R2 *ave*	Z	−10.98	6.84	309	−9.11
D751-R1.1	C	−10.48	7.96	273	−8.94
D757-R1.2		−10.67	7.49		
D757-R1.3		−10.97	7.45		
D757-R1.4		−10.79	7.17		
D757-R1 *ave*	Z	−10.81	7.37	291	−9.09
D757-R2.1		−10.75	6.91		
D757-R2.2		−10.80	6.71		
D757-R2.3		−10.95	6.48		
D757-R2 *ave*	D	−10.83	6.70	314	−8.93
$\delta^{13}C_{CO2}$ *ave*					−8.90
$\delta^{13}C_{CO2}$ *SD*					0.18

Note. ave, average of above analyses of a sample; *SD*, standard deviation.
[a]Temperature calculated using Friedman and O'Neil (1977) assuming vent fluid $\delta^{18}O$ = 1.49‰ VSMOW.

Zinc, Cu, Au, and Ag are, in general, lower at Auka than the more metal-rich chimneys from Alarcón Rise (Table 3 and Figures 12c and 12d and S3a). Calcite crystals formed in direct contact with hydrothermal fluid (chimney conduits or flange bottoms) show a range of $\delta^{13}C$ from −9.6 to −11.1‰ Vienna Pee Dee belemnite (VPDB) and $\delta^{18}O$ from 6.5 to 9.2‰ VSMOW (Table 4 and Figure 13). Calcite crystals from the inner calcite zone show a narrow range of $^{87}Sr/^{86}Sr$ values (0.706213 ± 0.000075; Table 5). Anhydrite from the outer anhydrite zone has $^{87}Sr/^{86}Sr$ values ranging from 0.70618 to 0.70857, and calcite intergrown with anhydrite has values ranging from 0.70677 to 0.70730 (Tables 5 and S3 and Figure 14). A single analysis of the Pb isotope composition of galena from sample D757-R2 shows that the Pb is more radiogenic than typical mid-ocean ridge basalt (MORB; $^{206}Pb/^{204}Pb$ = 18.762, $^{207}Pb/^{204}Pb$ = 15.614, and $^{208}Pb/^{204}Pb$ = 38.64; Figure S3e, Castillo et al., 2002).

Organic volatiles in the sediments include hydrocarbons from methane to heptane (C_1 to C_7) and many isomers (Table S4). Hydrocarbons heavier than n-heptane were not analyzed, although were very likely present due to the aromatic petroleum odor of the sediment. The $\delta^{13}C$ isotopic composition of the methane was ~ −28.6 to −31.4 ‰ VPDB.

4. Discussion

4.1. Locations of Hydrothermal Chimneys

Chimneys are restricted to the central third of the Alarcón Rise, with the active chimneys all in the southern part of that region and most associated with the fissure system of the youngest volcanic flow (Figures 1b and 2). The northern third of the segment includes a zone of evolved lavas, including a rugged rhyolite dome, which are interpreted to have formed by extreme fractional crystallization of MORB (Clague et al., 2018). It might be expected that the cooling and fractional crystallization that formed these evolved lavas would be related to extensive hydrothermal circulation and abundant hydrothermal deposits, yet no chimneys were mapped by the AUV surveys and no hydrothermal alteration zones were observed during numerous ROV dives. It is possible that hydrothermal deposits associated with the generation of these silicic lavas have been buried beneath younger basalt flows that onlap the eastern flank of the ridge of evolved lavas. Such a model, however, does not explain the absence of hydrothermal deposits on and west of the evolved lavas.
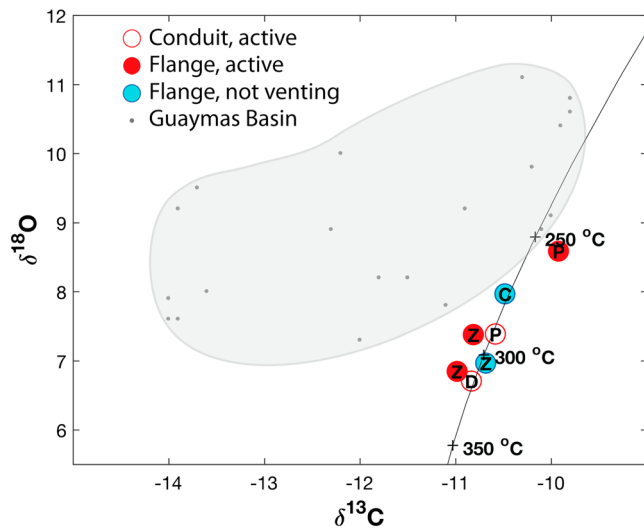
In the southern Pescadero Basin, the only mapped chimneys are found along the southwest margin of the basin, where faults provide permeability for fluid flow. Berndt et al. (2016) seismically imaged an actively venting mound in the northern Guaymas Basin that may be in a similar setting. The Guaymas mound is near the fault defining the rift axis, high on a block of thick chaotic sediments overlying reflectors interpreted to be magmatic intrusions. Chimneys are not evident in the AUV bathymetry in the Pescadero Basin axis (Figures 3a and 3b), nor associated with acoustic reflectors (Figure 3d) that could be buried lava flows or sills such as imaged at Guaymas Basin (Ondréas et al., 2018).

4.2. Hydrothermal Fluid Chemistry

Compositions of hydrothermal fluids and precipitates at sediment-starved mid-ocean ridges are controlled by the temperature and pressure regime, the composition of source rocks, and inputs of volcanic volatiles (Hannington et al., 2005; Monecke et al., 2016; Von Damm, 1990). Fluids can also react with rocks and sediment in the hydrothermal up-flow zone and therefore provide information about the underlying hydrothermal systems, such as evidence of volcanic activity or sediment involvement along flow pathways (e.g., Von Damm, 1990). Seafloor hydrothermal vent fields are generally classified based on the lithology through which the fluid passes, that is basalt-hosted or sediment-hosted (Hannington et al., 2005). The concentrations of certain elements or isotopic data can be used to help constrain such subsurface flow paths.

Figure 13. Plot of δ^{13}C (VPDB) versus δ^{18}O (VSMOW) from hand-picked calcite crystals growing on the inner lining of chimneys or the bottom surface of flanges, which formed in contact with hydrothermal fluids at the southern Pescadero Basin Auka field. Samples are symbolized by whether they were from pieces of conduit or flange, and actively venting or no longer venting, and labeled by chimney name. Most samples were run in replicate (Table 4); plotted data are averages. Gray points within enclosing gray field are data on carbonates from Guaymas Basin (Peter & Shanks, 1992) for comparison. The temperature curve is calculated for calcite in equilibrium with the measured vent fluid (δ^{18}O$_{water}$ = 1.49‰ VSMOW), using the fractionation curve of Friedman and O'Neil (1977) and the average calculated δ^{13}C of CO$_2$ in the fluid (δ^{13}C$_{CO2}$ = −9.0‰) using the fractionation equation of Bottinga (1968).

To characterize the source rocks within the Alarcón Rise and southern Pescadero Basin, Figures 10a–10e include end-member data from other well-characterized hydrothermal sites at mid-ocean ridges. New hydrothermal sites are continually being discovered and described in the liturature. The data plotted on Figure 10 do not include analyses from all reported mid-ocean ridge hydrothermal vents but cover the range of compositions observed from mid-ocean ridge hydrothermal fluids, with the exception of low salinity vents (<300 mmol/kg Cl) as no low salinity fluids were sampled at Meyibó or Auka vent fields. Mid-ocean ridge vent sites are subdivided as basalt-hosted, sediment-hosted, and ultramafic-hosted (Mottl, 2012). Basalt-hosted systems that have been interpreted to have also interacted with sediment in the subsurface are referred to here as sediment-influenced systems and include Endeavour (Butterfield, McDuff, Mottl, et al., 1994; Lilley et al., 2003; You et al., 1994) on the Juan de Fuca Ridge and Loki's Castle (Baumberger, Früh-Green, Dini, et al., 2016; Baumberger, Früh-Green, Thorseth, et al., 2016) on the Arctic Ridge. Basalt-hosted vent fields are represented by 11–13°N (Bowers et al., 1988; Palmer & Edmond, 1989; Spivack & Edmond, 1987), and 21°N (Campbell, Bowers, et al., 1988; Von Damm, Edmond, Grant, et al., 1985) on the EPR, MARK (Campbell, Palmer et al., 1988), TAG (Edmond et al., 1995), Lucky Strike (Von Damm et al., 1998), and Broken Spur (James et al., 1995) on the Mid-Atlantic Ridge, Sea Cliff (Von Damm et al., 2006) on the Gorda Ridge, Cleft (Damm & Bischoff, 1987; Palmer, 1991; Palmer & Edmond, 1989) and North Cleft (Butterfield & Massoth, 1994; Metz & Trefry, 2000; Trefry et al., 1994) on the Juan de Fuca Ridge, Piccard (McDermott et al., 2018; Webber et al., 2015) on the Mid-Cayman Rise, and Kairei (Gallant & Von Damm, 2006) and Edmond (Gallant & Von Damm, 2006) on the Central Indian Ridge. Sediment-hosted systems include Escanaba Trough (Campbell et al., 1994; Palmer, 1991; Von Damm et al., 2005; You et al., 1994) on the Gorda Ridge, Middle Valley (Butterfield, McDuff, Franklin, & Wheat, 1994) on the Juan de Fuca Ridge, and Guaymas Basin (Campbell & Edmond, 1989; Peter & Scott, 1988; Von Damm, Edmond, Measures, & Grant, 1985) in the Gulf of California. Ultramafic-hosted vent fields include high-temperature systems at Logatchev (Schmidt et al., 2007) and Rainbow (Charlou et al., 2002; Douville et al., 2002; Seyfried et al., 2011) on the Mid-Atlantic Ridge, and the Von Damm field on the Mid-Cayman Rise, which vents at intermediate temperatures (Hodgkinson et al., 2015; McDermott et al., 2015). Lost City (Kelley et al., 2001; Seyfried et al., 2015) near the Mid-Atlantic Ridge is also hosted by ultramafic rock and discharges low temperature, high pH fluids related to serpentinization of peridotite (Kelley et al., 2005).

4.2.1. Controls on Alarcón Rise Fluid Compositions

Vent fluids collected from the Meyibó field share many characteristics with the hydrothermal fields on the EPR and other basalt-hosted, sediment-starved mid-ocean ridge sites (Mottl, 2012; Von Damm, 1990). End-member (Mg-corrected) major and trace element fluid compositions and pH$_{25\,°C}$ at Meyibó are generally similar to fluid compositions reported from hydrothermal vents at 11, 13, and 21°N on the EPR (Figures 10a–10d). However, B concentrations are lower than most basalt hosted systems other than TAG (Figure 10b) and Cs is significantly enriched (Figure 10d). These differences could be due to differences in the source rocks, although Alarcón Rise basalts are not particularly Cs-rich (Clague et al., 2018), or potentially could relate to differences in water-rock ratio, as easily leached elements such as the alkalis can be enriched at low water-rock ratio (Palmer & Edmond, 1989; Seyfried et al., 1998; Von Damm, 1995, 2000). The δ^{18}O values of the vent fluids are elevated by about 2‰ relative to local bottom seawater values (Table 1), consistent with low water-rock ratio, with relatively unshifted δD, similar to most basalt-hosted vent fields (Shanks, 2001). The silica concentration for the 359 °C vent at

Table 5
Strontium Isotopes for Pescadero Basin Deposits[a]

Sample	Zone	n	Average ^{87}Sr/^{86}Sr	1 σ
D748-R3B	Inner zone calcite	10	0.70622	0.00002
D748-R3B	Outer zone anhydrite	14	0.7067	0.0004
D757-R2	Inner zone calcite	8	0.7062	0.0001
D757-R2	Outer zone anhydrite	18	0.7079	0.0006
D757-R2	Outer zone calcite	5	0.7071	0.0002

[a]Individual analytical points provided in Table S3.
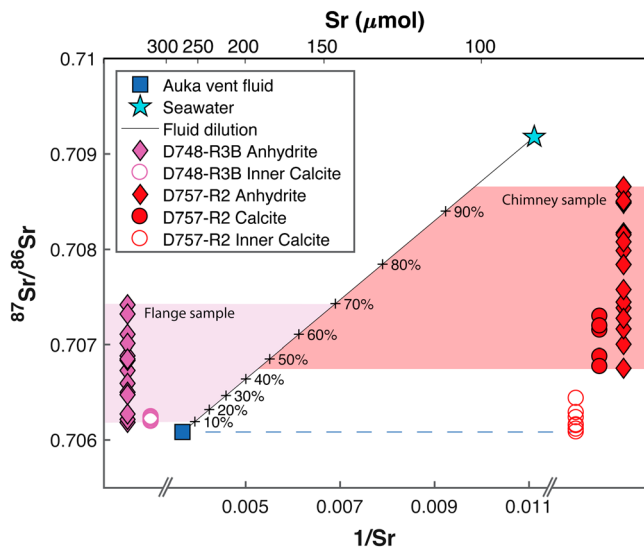
Figure 14. Calculated $^{87}Sr/^{86}Sr$ for conservative mixing between the Pescadero Basin Auka vent fluid and seawater. The Auka vent fluid is constrained by the lowest $^{87}Sr/^{86}Sr$ value (least contaminated through seawater mixing) measured from inner zone calcite (0.70608; Table S3) and the end-member vent fluid concentration (273 µmol/kg Sr; Table 1). The mixing line connecting them is annotated by the calculated dilution as percentage of seawater. The pink and red symbols indicate $^{87}Sr/^{86}Sr$ of outer zone crystals (from analysis of individual crystals of anhydrite and intergrown calcite; Table S3) and are plotted arbitrarily along the x axis. The colored fields bracket where the samples correspond with the fluid mixing line. The inner zone calcites are relatively homogeneous and show less mixing with seawater relative to the outer zone minerals. The higher and more variable $^{87}Sr/^{86}Sr$ values for crystals from the outer layers confirm that the outer zone forms from hydrothermal fluids mixed with as much as 94% seawater.

Meyibó is lower than that in the 340 °C vent, the reverse of what would be expected for prograde solubility. Silica solubility curves of Von Damm and Bischoff (1991) suggest that the higher temperature vent may record equilibration with silicate mineral at relatively shallow depth (~200 m) below the seafloor. The silica content of the lower temperature vent could reflect equilibrium in the source region at about 450 bar, similar to many other volcanic-hosted systems, suggesting circulation of fluids to depths near the base of the sheeted dikes in typical oceanic crust formed at intermediate spreading rates (Von Damm & Bischoff, 1991). The Meyibó fluids have similar CO_2 and CH_4 contents relative to other basalt-hosted systems (Figure 10e), and $^3He/^4He$ ratio (Table 2) that is within the range of values for a typical basalt-hosted system (Lupton et al., 2006). In most respects, the Alarcón Rise vent fluids are very similar to the majority of basalt-hosted systems, with the exception of those that have been affected by recent magmatic activity (e.g., Von Damm et al., 1995).

4.2.2. Controls on Pescadero Basin Fluid Compositions

The highest temperature measured at Auka was 291 °C and all of the vents emitted clear shimmering water, with little to no particulate plume. The $pH_{25 °C}$ of 6.3 measured onshore on Auka fluids (Table 1) may be slightly too high due to degassing of CO_2 after sample collection. We expect that the pH is likely to be closer to the pH of Guaymas Basin fluids (~6.0; Figure 10b). Chlorinity is 20% higher relative to seawater (Table 1 and Figure 10a). Several mechanisms for enhancing the salinity of seafloor hydrothermal fluids have been discussed in the literature (Berndt & Seyfried, 1990; Von Damm, 1988, 1990), but there is a general consensus that significant enrichment (or depletion) in salinity is an indication of high-temperature phase separation. The present fluid temperature is well below the boiling point at the seafloor pressure of 365 bars; thus, if the fluids have phase separated, then they have cooled substantially. The seafloor pressure is also significantly above the pressure at the critical point for seawater, so elevated salinity due to boiling is precluded, pointing to supercritical phase separation and condensation of a high salinity brine at temperatures in excess of 400 °C. The dissolved silica content of the Auka fluids (Table 1) falls below the quartz saturation curve of Von Damm and Bischoff (1991) at the measured T and P. However, silica solubility reverses above ~375 °C at the pressure of the Auka vents. It therefore appears likely that silica solubility reflects equilibrium at temperatures above ~450 °C at pressures determined by the depth of circulation, which is consistent with the high chloride value. The $^3He/^4He$ ratio of 7.7 R_a indicates a dominantly mantle-derived source for He (Spelz et al., 2015); however, the nature of the basement rocks and the extent of deep fluid circulation remain uncertain.

The Auka vent fluids overall (Figure 10) are similar to other sediment-hosted sites such as Escanaba Trough on the Gorda Ridge (Campbell et al., 1994; Palmer, 1991; Von Damm et al., 2005; You et al., 1994), and Middle Valley on the Juan de Fuca Ridge (Butterfield, McDuff, Franklin, & Wheat, 1994; Cruse et al., 2008), and seem most closely related to Guaymas Basin (Campbell & Edmond, 1989; Peter & Scott, 1988; Von Damm, Edmond, Measures, & Grant, 1985). The southern Pescadero Basin is blanketed with thick sediments (Figure 3), and the vent fluids show the characteristics of having interacted with sediment, including the relatively high pH and enrichments in highly soluble elements such as B and alkalis, relative to Alarcón Rise and other basalt- and ultramafic-hosted hydrothermal systems (Figures 10b and 10c). The high Li, Rb, Cs, and B contents (Table 1) fall on the trends defined by sediment-influenced vent fluids in Escanaba Trough and Guaymas Basin (Figure 10c). However, elevated cation concentrations are also present in high chloride fluids, such as at basalt-hosted Cleft and North Cleft (Figure 10a). Chloride normalized Rb versus Li also shows the clear distinction between basalt- and ultramafic-hosted systems and those that have interacted with sediment. The very high Cs concentration in Auka fluids (Table 1) and abundance of Cs relative to other highly soluble elements are similar to fluids from sediment-hosted Escanaba Trough (Figure 10d). Trace metal contents of Fe, Mn, and Cu are lower than those in Alarcón fluids, consistent with the higher pH and lower

temperature of the Pescadero fluids, but Zn concentrations are similar to those in Alarcón fluids (Table 1). Pescadero vent fluids have slightly elevated values of $\delta^{18}O$ (1.49‰ VSMOW) and δD (3.7‰ VSMOW; Table 1) consistent with interaction with sediment (Shanks, 2001).

The Auka fluids and sediments have high dissolved gas concentrations, including higher-order hydrocarbons (Tables 2, S4). The low ratio of CH_4 relative to higher order hydrocarbons (Tables 2 and S4) is a characteristic of thermogenic hydrocarbon generation as a result of enhanced thermal maturation of organic matter during fluid/sediment interaction (e.g., Simoneit et al., 1992). The elevated CO_2 and CH_4 contents of Auka fluids plot with other sediment-hosted sites (Figure 10e). We calculate the $\delta^{13}C$ of dissolved CO_2 in the vent fluid that would be in equilibrium with the average measured $\delta^{13}C$ value of calcite (-8.9‰ VPDB; Table 4) by applying the carbon isotope fractionation equation of Bottinga (1968). The temperature for each sample was constrained using the oxygen isotope fractionation curve of Friedman and O'Neil (1977) applied to the average $\delta^{18}O$ value for each calcite sample (Table 4) and the measured $\delta^{18}O$ value of the end-member Auka vent fluid (1.49‰ VSMOW; Table 1). The results are compared to similar data from Guaymas Basin (Peter & Shanks, 1992) in Figure 13. The average calculated $\delta^{13}C$ of dissolved CO_2 (-9.0‰ VSMOW $\pm$ 0.18 1σ) at Auka is similar to the value for Guaymas Basin fluid (-8.5‰) calculated by Peter and Shanks (1992), consistent with remobilized sedimentary carbonate, with a substantial contribution from the thermal breakdown of isotopically light sedimentary organic carbon. The contribution of organic carbon can be estimated by isotope mass balance, assuming that the values of inorganic carbon (-2.2‰) and organic carbon (-21‰) measured in Guaymas sediment by Seewald et al. (1994) also apply at Pescadero Basin, and suggests that approximately 36% of the CO_2 is derived from organic matter. Given the low concentration of CO_2 in typical basalt-hosted vent fluids, contribution of volcanically derived carbon is insignificant. The southern Pescadero Basin is at a depth that is near to the carbonate compensation depth in the eastern Pacific (Chen et al., 1988), although we are unaware of any data on bottom water compositions at ~3,800 m in the Gulf of California that could be used to calculate carbonate saturation state. Pelagic sediment deposited in this basin would be expected to be low in inorganic carbonate. Carbonate that contributes to the dissolved CO_2 in the vent fluid could have been delivered to the basin by turbidity currents sourced from shallower depths. Alternatively, deeper sediment below the active vent field may have been deposited in shallower water, prior to tectonic subsidence due to extention and formation of the pull-apart basin.

The Auka vent fluids are inferred to have a $^{87}Sr/^{86}Sr$ value of 0.70608, the value of the least radiogenic, and therefore least contaminated by seawater mixing, Sr isotope ratio measured in calcite that formed in contact with hydrothermal fluid from the interior of the hydrothermal chimney sample D757-R2 (Table S3 and Figure 14). This is more radiogenic than the strontium isotopic ratio of Guaymas Basin vent fluid (0.70528; Piepgras & Wasserburg, 1985). In both Auka and Guaymas, the strontium isotopic ratios are significantly more radiogenic than typical basalt-hosted systems, which often have strontium isotopic ratios similar to the basaltic host rocks (Von Damm, 1995). This is due to significant contribution from sedimentary sources.

4.3. Hydrothermal Deposits

The pH and elemental composition of the hydrothermal fluids influence the composition of the hydrothermal deposits, but source rock composition generally plays the dominant role. Sediment-hosted seafloor hydrothermal systems tend to show higher concentrations of Pb, Sb, As, and Ag compared to basalt-hosted systems, which tend to be rich in Cu and Zn (e.g., Hannington et al., 2005). Hydrothermal deposits on the Alarcón Rise and in the southern Pescadero Basin are consistent with that pattern.

4.3.1. Alarcón Rise Hydrothermal Deposits

The vigorously active chimneys on the Alarcón Rise are black smokers, like elsewhere on the EPR, and precipitates emanating from slender orifices at the tops and out the sides build Fe-Zn-Cu-rich sulfide chimney structures (Figures 11a and 11b and 12a and 12b). The samples tend to be bimodal in their base-metal contents, being either high Zn or high Cu (Table 3 and Figure 12c). A somewhat higher proportion of samples rich in Zn was collected from inactive chimneys (Table 3 and Figure 12b) and rich in Cu from active chimneys. This likely represents some sampling bias as narrow chimney tops are more easily and more commonly sampled by submersible and the interiors of large edifices or mounds are generally not available for sampling. Given that the fluids would be expected to cool as hydrothermal activity wanes, it would be expected that the final stage of chimney growth would include more Zn-rich precipitates as zinc can be transported in solutions at lower temperature than copper (Hannington et al., 1995). Similar sampling bias likely exists at most

hydrothermal fields, so our data set should be comparable with the compilations of geochemical data presented in Hannington et al. (2005) and Monecke et al. (2016), who discuss the difficulty of assessing true resource grade and tonnage in the absence of three dimensional sampling provided by core drilling.

The Alarcón Rise fields are built on lava flows, and most of the samples have little Pb, as expected due to the low abundance of Pb in MORB. However, Pb can also be remobilized by low-temperature fluids through zone-refining and enriched in the outer-most late-stage, lower temperature mineralization (Hannington et al., 1995). This may explain the anomalous Pb-rich (1.9 wt%) composition of sample D392-R8 from the Meyibó field (Table 3 and Figures 4b and 12a and 12d). The sample was broken from a small Zn-rich spire near the base of an inactive 8-m-high chimney, below which tubeworms and clams grew in low-temperature fluids that vented from cracks in the lava (Figure S2b). This sample also has high Ag (872 ppm) and elevated Au (863 ppb) contents, as would be expected from local redistribution of base and precious metals due to zone-refinement from older sulfide deposited in the chimney interior and reprecipitation at a lower temperature, white-smoker-like vent at a mid-ocean ridge.

The longevity of hydrothermal structures and flow at these sites is difficult to quantify but can be estimated qualitatively in several ways. One measure is the size of the deposit. The chimneys at the off-axis Tzab-ek field are taller than the others at Alarcón. It is also differs from the on-axis vent fields in that the chimneys rise from a sulfide mound formed of chimney talus, whereas the other fields show chimneys growing directly on the basaltic substrate. The volume of deposited sulfide indicates that the Tzab-ek field has been hydrothermally active for a longer period, or precipitated sulfide at a much higher rate, than the on-axis Alarcón fields. It is not clear if the Tzab-ek field first formed on-axis and continued to grow as it drifted to its present location. The Tzab-ek field may have a deeper, regional source of heat, or more permeability pathways provided by the bounding fault may allow continued extraction of heat from the axial magma chamber. In either case, the underlying hydrothermally altered rocks will have undergone more cumulative water-rock reaction compared to the nearby on-axis fields.

On the Endeavour Segment of the Juan de Fuca Ridge, chimneys within active fields were determined to be at least 2,200 years old, and inactive chimneys outside the graben were up to 5,800 years old (Jamieson et al., 2013). Those active chimneys grow to 45 m tall, and the deposits are Si-rich, to 28 wt%, which permits the growth of the unusually large edifices and lateral flanges (Tivey et al., 1999) and may contribute to their stability even after they become inactive. The Tzab-ek chimneys have developed flanges, yet as with most of the other Alarcón chimneys, they have low Si contents (<1 wt%; Table 3). While up to 33 m in height, the chimneys at Tzab-ek are at most 8 m in diameter, and the ~5-m-thick deposit beneath them may be due to collapse of unstable chimneys over time.

The age of the inactive chimneys in the ICF (Figure 8) is partly constrained by the age of the underlying lava flows, which are up to a thousand years old (Clague et al., 2018). That chimneys are still standing up to 15 m high and are relatively unaltered (Figures 6b and S2f) suggests either that they are youthful chimneys on older substrate or that chimneys may take many hundreds of years to oxidize and disintegrate after fluid discharge has ceased. Samples from ICF generally have low calcium contents (and hence low anhydrite abundance), and only one sample was observed to still contain anhydrite, which dissolves from inactive chimneys due to retrograde solubility (Blount & Dickson, 1969). Fe-rich sulfides (e.g., pyrrhotite and pyrite) are easily oxidized in seawater (Figure 6b), and the oxidation of pyrite produces sulfuric acid that accelerates weathering of the sulfides, whereas weathering of sphalerite does not (Seal & Hammarstrom, 2005). However, it is not clear if this difference contributes to the preservation of chimney structures at the ICF.

4.3.2. Pescadero Basin Hydrothermal Deposits

High-temperature fluids (to 291 °C) in the Auka field in the Pescadero Basin are precipitating nearly pure calcite. Figure 15 shows an interpretive cross section based on petrographic observations (Figures 11d–11h) that is applicable to the actively venting conduits and flanges of the large chimneys. Coarse-grained, euhedral, bladed calcite crystals form in contact with the high-temperature fluids, whether in the interior of an active conduit or on the underside of a flange. The inner calcite is inferred to have formed by direct precipitation from hydrothermal fluid based on statistically insignificant variation of $^{87}Sr/^{86}Sr$ values (Tables 5 and S3 and Figure 14) and the $\delta^{13}C$ and $\delta^{18}O$ values (Table 4), which are consistent with precipitation of calcite at temperatures near those measured in the active vents (Figure 13). The exterior chimney walls and the upper surfaces of flanges, which are in contact with cold seawater (2 °C) containing sulfate and Mg, are dominantly
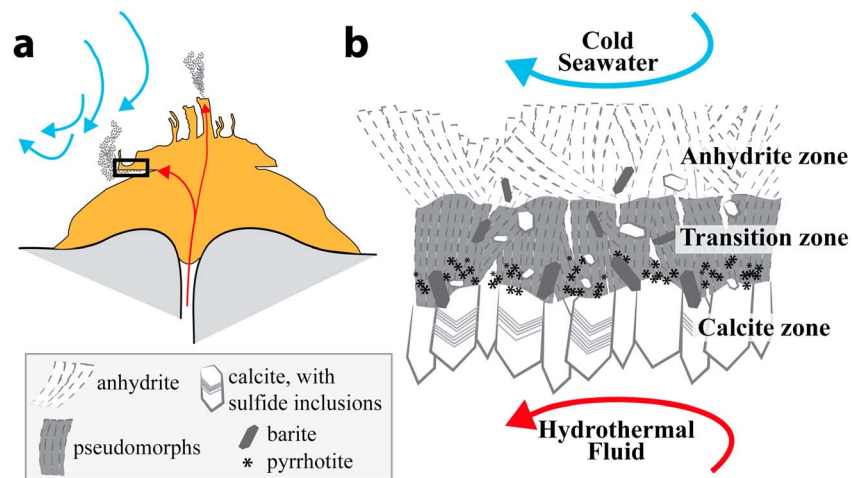
Figure 15. Schematic of Pescadero Basin Auka chimney development model based on backscattered electron and microscopic analyses of deposit samples. (a) Cross section through a carbonate mound that has a flange, outlined by black box and illustrated in (b). Hydrothermal fluids (red arrows) rise through conduits and exit through slender orifices and underneath flanges, where it is cooled by seawater (blue arrows). (b) Cross section through an idealized flange. The outer anhydrite zone is in contact with cold seawater (Figure 11g). The anhydrite grows as dendritic crystals in an irregular fabric and has a felted appearance. Disseminated crystals of barite and calcite are concentrated near the transition zone. The transition zone is where hydrothermal fluids permeate, dissolving the anhydrite crystals. Mixing between silica-rich hydrothermal fluid and cold Mg-bearing seawater leads to precipitation of Mg-rich clays that form pseudomorphs of the anhydrite. Cooling of the hydrothermal fluid also deposits sulfides, dominantly thin plates of hexagonal pyrrhotite (Figure 11h). Fine calcite, botryoidal amorphous silica, and Mg smectite are disseminated through the layer (Figure 11g). The calcite zone is in the interiors of conduits or underneath flanges, in contact with the hydrothermal fluids. Chevron patterns on the large, bladed crystals (Figure 11f) are inclusions of sulfide, dominantly pyrrhotite, with trace chalcopyrite, sphalerite, and galena.

composed of anhydrite, with less abundant disseminated calcite, barite, and minor amounts of sulfide minerals. Between the interior calcite and exterior anhydrite layers, a transition zone forms where hydrothermal fluid permeates and mixes with seawater through advection or diffusion (Tivey, 1995). The Mg-rich clay deposited in this zone often pseudomorphs bladed anhydrite that was initially overgrown by Mg-clay $\pm$ sulfide, and later dissolved. The dissolved anhydrite is later infilled with Mg-clay or fine-grained calcite, which poorly preserves the original anhydrite texture (Figure 11g).

The $^{87}Sr/^{86}Sr$ isotope ratios of the calcite and anhydrite crystals in the transition and outer zones are generally higher and more variable than those of the inner zone calcites (Tables 5 and S3) and can be used to quantify local mixing prior to their precipitation. Figure 14 shows a calculated mixing line between vent fluid Sr and seawater Sr. Strontium isotope values of calcite and anhydrite from inner and outer zones of a flange sample (D748-R3B) and a chimney sample (D757-R2) are plotted against 1/Sr. $^{87}Sr/^{86}Sr$ values of calcite from the inner zone, formed in direct contact with hydrothermal vent fluid, show the least evidence of mixing with seawater but are consistent with minor entrainment of seawater-derived strontium in chimney interiors or flange pools. Relative to the mixing line, the $^{87}Sr/^{86}Sr$ values in anhydrite from the upper surface of flange sample D748-R3B suggest formation from hydrothermal fluid mixed with 10% to 70% seawater, and values in anhydrite from the outside of chimney wall sample D757-R2 suggest more extensive mixing of the fluid with 45 to 94% seawater.

Although calcite dominates these deposits, some polymetallic sulfides exist. Sulfide minerals are most abundant in the chimney transition zone but are generally present in trace amounts. The dominance of pyrrhotite indicates low fS_2-fO_2 relative to basalt-hosted deposits, which often contain pyrite, especially in the more mature deposits (Hannington et al., 2005). Chalcopyrite-isocubanite, sphalerite, and galena are present in similar amounts and the deposits plot in the Pb-rich portion of a Cu-Zn-Pb diagram (Figure 12c), similar to Guaymas Basin or Escanaba Trough sulfides (Zierenberg et al., 1993). Sample D757-R2 is somewhat unusual in having abundant sulfide (Table 3) as chalcopyrite and galena, with no sphalerite, and indicates that the Auka fluids are capable of transporting and depositing significant amounts of base metal sulfides at times.

A sedimentary source for lead is indicated by a single analysis of the Pb isotope composition of galena from sample D757-R2 (Table 3). The galena has a more radiogenic value than basaltic rocks from the Alarcón Rise or vent fluids from 21°N EPR. The Auka galena is not as radiogenic as Escanaba Trough or Middle Valley sulfides and plots closer to the Pb in Guaymas Basin vent fluids, consistent with derivation from Gulf of California sediments with a similar source of Pb (Chen et al., 1986).

The composition of the C_2-C_7 hydrocarbons in the sediments (Table S4) is consistent with the formation of petroleum condensates and similar to those found in the Guaymas Basin (Simoneit et al., 1988). The hydrocarbons present are clearly derived from a thermogenic source ($C_1/C_2 + C_3$ ratios of <10; Bernard et al., 1976) consistent with hydrothermal fluids interacting with sedimentary organic matter at temperatures exceeding at least ~50 °C, the onset of petroleum generation (Tissot & Welte, 1984). The methane carbon isotopic composition (−28.6 to −31.4 ‰; Table S4) affirms high-temperature hydrocarbon production. The relative ^{12}C depletion suggests that the methane was formed at temperatures higher than ~190 °C; however, the presence of other wet gases (C_2-C_7) suggests that the temperature could not exceed ~190 °C for prolonged time intervals, as above this temperature these compounds will be thermally cracked. We suggest that the hydrothermal plumbing system is prone to create steep localized temperature gradients that subject the sediment to wide-ranging petroleum-forming temperatures resulting in a rich mixture of petroleum compounds.

4.3.3. Comparison of Pescadero Basin With Guaymas Basin Hydrothermal Systems

There are many similarities between the hydrothermal systems in southern Pescadero Basin and in Guaymas Basin, which are both hosted in sediment-covered pull-apart grabens in the Gulf of California transform fault system (Figure 1). Guaymas chimneys are described as *pagoda-shaped* (Von Damm, 1990), with many flanges, which are also common at Auka (Figures 6b and 6c). As in our model for Auka (Figure 15), anhydrite is deposited in Guaymas where hydrothermal fluids are in contact with seawater sulfate, and calcite is deposited where high-temperature fluids are insulated from seawater (Peter & Scott, 1988). Both deposits are polymetallic, with pyrrhotite as the generally dominant sulfide mineral. The fluids at both sites are slightly alkaline, enriched in B and alkalis. Auka is also similar to Guaymas in having elevated CO_2 and CH_4 contents (Table 2 and Figure 10e), high concentrations of higher order C_2-C_4 gases, and low ratios of CH_4 relative to higher order hydrocarbons (Tables 2 and S4), all indications of hydrothermal fluid interaction with organic matter in the underlying sediment (e.g., Simoneit et al., 1992). Carbon isotope values at both sites indicate derivation from a mixture of sedimentary carbonate and oxidized organic matter. Sedimentary sources are also indicated by the Sr and Pb isotope ratios of hydrothermal minerals. Both sites also have $^3He/^4He$ consistent with interaction with basaltic rocks that are probably the heat source driving high temperature fluid circulation.

In summary, the Auka vent fluids are consistent with other sediment-hosted vent fluids and are compositionally most similar those from Guaymas Basin. Von Damm, Edmond, Measures, and Grant (1985) proposed that the chemistry and isotopic values of Guaymas Basin fluids indicate initial high temperature interaction with oceanic crust producing fluids similar in composition to the 21°N EPR fluids, followed by fluid-sediment interaction in the fluid up-flow zone that dissolves carbonate and thermally cracks immature organic carbon, raising the pH and adding ammonium and hydrocarbons to the fluids. It has also been proposed (Seewald et al., 1994; Von Damm, Edmond, Measures, & Grant, 1985) that interaction of a 21°N-like vent fluid with the sediment column is likely to result in the deposition of the metal sulfides in the subsurface prior to venting to the seafloor. The same model likely applies to the Auka system.

An important difference between the Guaymas system and southern Pescadero Basin is the relative paucity of sulfide deposited on the seafloor. The composition of the Auka vent fluids suggests that they phase separated at high-temperature, supercritical conditions (see section 4.2.2), and there is nothing to suggest that the source fluids were incapable of transporting significant quantities of dissolved metals. It remains an open question as to why the majority of metals appear to precipitate below the seafloor in the Auka system. The system may have had more extensive interaction with the sediment that titrated the acidity of the basement-derived fluid due to reaction with sedimentary carbonate, which would promote the deposition of sulfide minerals. Flow through the sedimentary section could also result in conductive cooling and/or mixing with cooler, high pH pore fluids. The maximum present-day vent temperatures at Auka are approximately 25 °C lower than those in the southern Guaymas Basin (315 °C; Von Damm, Edmond, Measures, & Grant, 1985). The calcite depositional temperature, calculated using the oxygen isotope fractionation (Friedman & O'Neil, 1977), the measured oxygen isotope value in calcite, and assuming that the oxygen isotope value

of vent fluid has remained constant ($\delta^{18}O = 1.49‰$), ranges from the measured vent temperature of 291 up to 314 °C, with the exception of sample D748-R2, which gave a temperature of 256 °C (Table 4). Sample D748-R2 was collected from the leading edge of an active flange and may record a lower temperature due to incorporation of seawater into the turbulent flange overflow. As discussed below, the evidence suggests that Auka has been active for a long time, and it may be in a stage of thermal decline. However, given the very large amount of hydrothermal calcite that has been, and continues to be, deposited in the Auka vent field, it seems highly likely that the area is underlain by a large polymetallic replacement deposit, an hypothesis that should be investigated using geophysical techniques and ultimately tested by scientific ocean drilling.

Another difference between Guaymas Basin and the southern Pescadero Basin is the lack of observed methane bubble trains venting from the seafloor in the Auka field and their common occurrence in the Guaymas Basin field (Berndt et al., 2016; Ondréas et al., 2018; Paull et al., 2007). This most likely results from the much greater depth in Pescadero Basin, which requires significantly higher gas concentrations to achieve supersaturation. Methane seeps at Guaymas are often associated with circular collapse pits in the sediment (Ondréas et al., 2018) surrounded by microbially-generated carbonate hard grounds (Paull et al., 2007). These low-temperature seep areas often support chemosynthetic faunal communities (Soule et al., 2018). We note that similar scale collapse pits or pockmarks (Kluesner, 2012) are evident in the sediment-filled rift basin of southern Pescadero Basin (Figure 3a), but AUV side scan sonar evidence of carbonate hard ground is lacking and these areas have yet to be explored for seeps.

Other than Guaymas, the only other large hydrothermal field of carbonate chimneys known from mid-ocean ridge settings is the Lost City field, which is 15 km off-axis of the Mid-Atlantic Ridge (Kelley et al., 2001) and considered to be a low-temperature ultramafic-hosted site. The high pH fluids at Lost City are formed by serpentinization reactions (Kelley et al., 2001; Seyfried et al., 2015) and precipitate aragonite-calcite-brucite chimneys. Auka fluid does not resemble Lost City's fluids in terms of temperature, pH, or composition (Figure 10). In contrast with the low-temperature ultramafic-hosted site, high-temperature ultramafic-hosted hydrothermal fluids tend to lie on the same trends as the basalt-hosted sites and are distinguished by the high relative contribution of H_2 to the gas compositions (Figure 10e) due to the highly reduced nature of fluids that have interacted with ultramafic rocks. However, vent fluids from the recently described Piccard vent field on the Mid-Cayman Rise also have high H_2 concentrations attributed to high temperature (>400 °C) basalt-seawater interaction (McDermott et al., 2018).

Although both Guaymas Basin and southern Pescadero Basin are interpreted as pull-apart or fault-termination basins where new oceanic crust is being generated, definitive evidence of magmatic spreading in southern Pescadero Basin is lacking at present. We are unaware of any magnetic profile data that could be used to infer the presence of basaltic rocks in the subsurface. The MBARI AUV seismic reflection profiles across the southern Pescadero Basin confirm that it is a sediment-filled graben bounded by relatively recent normal faulting (Figure 3b) but do not preclude an origin as an amagmatic pull-apart basin. A hard acoustic reflector can be seen beneath 20–50 m of sediment cover on most of the seismic profiles; however, it is unknown if it is recently formed oceanic crust. AUV side scan sonar does not image any surface lava flows, and all strong returns are associated with features with topographic relief, including fault scarps (Figure 3d), which have not been investigated by ROV to see if they expose young basalt. The vent field is perched on the up-thrown block of the innermost rift-bounding normal fault, which probably provides permeability for fluid flow, but basement was not imaged beneath it (Figures 3c and 3d).

Sediment-covered hills that were likely uplifted by sills were mapped just north of the Auka vent field (Figure 3a), but the vent field is not spatially associated with these features. Einsele et al. (1980) established the importance of sill intrusion in controlling hydrothermal circulation in the Guaymas Basin. More recently, Berndt et al. (2016) document the association of sills emplaced in the upper sedimentary section of Guaymas Basin with both low-temperature hydrothermal seeps and higher temperature vent fields in Guaymas Basin. Seismic surveys capable of imaging sills have not been conducted in the Pescadero Basin. Sediment hills uplifted by sills intruded near the sediment-basalt interface at sediment-covered spreading centers are spatially associated with high-temperature hydrothermal systems at Escanaba Trough (Denlinger & Holmes, 1993; Zierenberg et al., 1993) and Middle Valley (Zierenberg et al., 1998). Low-temperature hydrothermal seeps have recently been described from sediment covered, transtensional transform fault zones adjacent to Alarcón Rise (Figure 1b; Clague et al., 2018). Sill intrusion is likely a fundamental aspect of the creation

and architecture of oceanic crust in sediment covered spreading centers (Zierenberg et al., 1993, 1998) where it may provide a control on the location of hydrothermal venting.

Carbonate talus samples collected from the Auka vent field show evidence of dissolution, the chimneys are delicate, and calcite deposition does not appear to be rapid, yet substantial amounts of hydrothermal calcite have accumulated on the seafloor. Carbonate crusts are prevalent in flat, sediment covered areas between the large carbonate mounds, and seismic reflection lines show hard substrate between the mounds. Sediments clearly onlap the mounds and have buried their bases (Figures 3c and 3d). It is therefore likely that the mounds represent only a fraction of the total carbonate accumulated at this site. The fluids venting at the site also appear to have cooled by ~150 °C from the temperature at which phase separation apparently occurred. All of the evidence taken together suggests that the vent field is substantial in terms of the mass of carbonate precipitated, and long lived.

5. Conclusions

Our work has demonstrated that high-resolution mapping using AUVs is an effective and efficient approach to discovering and characterizing active and inactive fields of hydrothermal chimneys. The entire Alarcón Rise spreading segment has been mapped at high resolution with the discovery of four active high-temperature fields and an extensive field of inactive chimneys. The active Meyibó, Pericú, and Ja Sít vent fields are located on or near the spreading axis in the magmatically most robust segment of the ridge, and the older, more mature Tzab-ek vent field occurs ~850 m off-axis. Fluids have been sampled from two hydrothermal vents in Meyibó vent field, but no fluid samples have been taken from the other three vent fields. Comparison between fluid chemistry of the younger, on-axis vent field with Tzab-ek may help illuminate the role of integrated water/rock ratio controls on hydrothermal fluid chemistry, particularly the concentrations of highly soluble elements such as boron and alkali metals. An inactive chimney field occurs along a section of the ridge that has not experienced recent volcanic eruptions.

The large, sediment-hosted high-temperature Auka vent field was discovered at ~3,700 m depth in the southern Pescadero Basin. Auka differs from other mid-ocean ridge vent fields in that it dominantly forms large calcite mounds and chimneys with only minor sulfide mineralization. Auka fluids have compositions similar to those from other sediment-hosted mid-ocean ridge vent fields, especially Guaymas Basin. Guaymas chimneys contain abundant polymetallic sulfide in addition to hydrothermal calcite, whereas the Auka chimneys are nearly pure calcite. The paucity of sulfide phases suggests subsurface deposition of a large sulfide-replacement deposit and makes Auka distinct from most other high temperature vent fields. The substantial carbonate deposits indicate that Auka is a long-lived vent field requiring extensive integrated water/rock reaction in the subsurface, making this a prime target for scientific drilling to investigate the formation of subseafloor polymetallic replacement deposits.

The Alarcón Rise and southern Pescadero Basin vent fields occur midway between well-described vent faunal communities at 21°N and Guaymas Basin, providing important data points to evaluate controls on vent fauna distribution and endemism. Goffredi et al. (2017) have shown that the Auka vent field in Pescadero Basin contains a unique mix of high temperature and seep related vent fauna.

References

Baker, E. T., German, C. R., & Elderfield, H. (1995). Hydrothermal plumes over spreading-center axes: Global distributions and geological inferences. In S. E. Humphris, R. A. Zierenberg, L. S. Mullineaux, & R. E. Thomson (Eds.), *Seafloor hydrothermal systems—Physical, chemical, biological and geological interactions*, *American Geophysical Union Monograph* (Vol. 91, pp. 47–71). Washington, DC.

Baumberger, T., Früh-Green, G. L., Dini, A., Boschi, C., van Zuilen, K., Thorseth, I. H., & Pederson, R. B. (2016). Constraints on the sedimentary input into Loki's Castle hydrothermal system (AMOR) from B isotope data. *Chemical Geology*, *443*, 111–120. https://doi.org/10.1016/j.chemgeo.2016.09.026

Baumberger, T., Früh-Green, G. L., Thorseth, I. H., Lilley, M. D., Hamelin, C., Bernasconi, S. M., et al. (2016). Fluid composition of the sediment-influenced Loki's Castle vent field at the ultra-slow spreading Arctic Mid-Ocean Ridge. *Geochimica et Cosmochimica Acta*, *187*, 156–178.

Beaulieu, S. E., Baker, E. T., German, C. R., & Maffei, A. (2013). An authoritative global database for active submarine hydrothermal vent fields. *Geochemistry, Geophysics, Geosystems*, *14*, 4892–4905. https://doi.org/10.1002/ggge.20296

Bernard, B. E., Brooks, J. M., & Sackett, W. M. (1976). Natural gas seepage in the Gulf of Mexico. *Earth and Planetary Science Letters*, *31*(1), 48–54. https://doi.org/10.1016/0012-821X(76)90095-9

Berndt, C., Hensen, C., Mortera-Gutierrez, C., Sarkar, S., Geilert, S., Schmidt, M., et al. (2016). Rifting under steam—How rift magmatism triggers methane venting from sedimentary basins. *Geology*, *44*(9), 767–770. https://doi.org/10.1130/G38049.1

Berndt, M. E., & Seyfried, W. E. Jr. (1990). Boron, bromine, and other trace elements as clues to the fate of chlorine in mid-ocean ridge vent fluids. *Geochimica et Cosmochimica Acta*, *54*(8), 2235–2245. https://doi.org/10.1016/0016-7037(90)90048-P

Blount, C. W., & Dickson, F. W. (1969). The solubility of anhydrite (CaSO₄) in NaCl-H₂O from 100 to 450°C. *Geochimica et Cosmochimica Acta*, *33*, 227–245.

Bottinga, Y. (1968). Calculation of fractionation factors for carbon and oxygen isotopic exchange in the system calcite-carbon dioxide-water. *The Journal of Physical Chemistry*, *72*(3), 800–808. https://doi.org/10.1021/j100849a008

Bowers, T. S., Campbell, A. C., Measures, C. I., Spivack, A. J., Khadem, M., & Edmond, J. M. (1988). Chemical controls on the composition of vent fluids at 13°–11°N and 21°N, East Pacific Rise. *Journal of Geophysical Research*, *93*, 4522–4536. https://doi.org/10.1029/JB093iB05p04522

Butterfield, D. A., & Massoth, G. J. (1994). Geochemistry of north cleft segment vent fluids: Temporal changes in chlorinity and their possible relation to recent volcanism. *Journal of Geophysical Research*, *99*, 4951–4968. https://doi.org/10.1029/93JB02798

Butterfield, D. A., McDuff, R. E., Franklin, J., & Wheat, C. G. (1994). Geochemistry of hydrothermal vent fluids from Middle Valley, Juan de Fuca Ridge. In M. J. Mottl, E. E. Davis, A. T. Fisher, & J. F. Slack (Eds.), *Proceedings of the Ocean Drilling Program, Scientific Results* (Vol. 139, pp. 395–410). College Station, TX: Ocean Drilling Program.

Butterfield, D. A., McDuff, R. E., Mottl, M. J., Lilley, M. D., Lupton, J. E., & Massoth, G. J. (1994). Gradients in the composition of hydrothermal fluids from the Endeavour Segment vent field: Phase separation and brine loss. *Journal of Geophysical Research*, *99*, 9561–9583. https://doi.org/10.1029/93JB03132

Campbell, A. C., Bowers, T. S., Measures, C. I., Falkner, K. K., Khadem, M., & Edmond, J. M. (1988). A time series of vent fluid compositions from 21°N, East Pacific Rise and the Guaymas Basin, Gulf of California. *Journal of Geophysical Research*, *93*, 4537–4549. https://doi.org/10.1029/JB093iB05p04537

Campbell, A. C., & Edmond, J. M. (1989). Halide systematics of submarine hydrothermal vents. *Nature*, *342*(6246), 168–170. https://doi.org/10.1038/342168a0

Campbell, A. C., German, C. R., Palmer, M. R., Gamo, T., & Edmond, J. M. (1994). Chemistry of hydrothermal fluids from Escanaba Trough, Gorda Ridge. *U.S. Geological Survey Bulletin*, *2022*, 201–221.

Campbell, A. C., Palmer, M. R., Klinkhammer, G. P., Bowers, T. S., Edmond, J. M., Lawerence, J. R., et al. (1988). Chemistry of hot springs on the Mid-Atlantic Ridge. *Nature*, *335*(6190), 514–519. https://doi.org/10.1038/335514a0

Caress, D., Troni, G., Clague, D., Paduan, J., Martin, J., Thomas, H., et al. (2015). Detection of active hydrothermal vent fields in the Pescadero Basin and on the Alarcón Rise using AUV multibeam and CTD data, Abstract OS23C-2027 Presented at the AGU Fall Meeting, San Francisco, CA, December 14–18.

Caress, D. W., Clague, D. A., Paduan, J. B., Martin, J. F., Dreyer, B. M., Chadwick, W. W. Jr., et al. (2012). Repeat bathymetric surveys at 1-metre resolution of lava flows erupted at Axial Seamount in April 2011. *Nature Geoscience*, *5*(7), 483–488. https://doi.org/10.1038/ngeo1496

Caress, D. W., Thomas, H., Kirkwood, W. J., McEwen, R., Henthorn, R., Clague, D. A., et al. (2008). High-resolution multibeam, sidescan, and subbottom surveys of seamounts, submarine canyons, deep-sea fan channels, and gas seeps using the MBARI AUV *D. Allan B.* In J. R. Reynolds & H. G. Greene (Eds.), *Marine Habitat Mapping Technology for Alaska* (pp. 47–70). Alaska Sea Grant College Program, University of Alaska, Fairbanks. https://doi.org/10.4027/mhmta.2008.04

Castillo, P., Hawkins, J., Lonsdale, P., Hilton, D., Shaw, A., & Glascock, M. (2002). Petrology of Alarcón Rise lavas, Gulf of California: Nascent intracontinental ocean crust. *Journal of Geophysical Research*, *107*(B10), 2222. https://doi.org/10.1029/2001JB000666

Charlou, J. L., Donval, J. P., Fouquet, Y., Jean-Baptiste, P., & Holm, N. (2002). Geochemistry of high H₂ and CH₄ vent fluids issuing from ultramafic rocks at Rainbow hydrothermal field (36°14′N, MAR). *Chemical Geology*, *19*, 345–359.

Chen, C. T. A., Feely, R. A., & Gendron, J. F. (1988). Lysocline, calcium carbonate compensation depth and calcareous sediment in the North Pacific Ocean. *Pacific Science*, *42*, 237–252.

Chen, J. H., Wasserburg, G. J., Von Damm, K. L., & Edmond, J. M. (1986). The U-Th-Pb systematics in hot springs on the East Pacific Rise at 21°N and Guaymas Basin. *Geochimica et Cosmochimica Acta*, *50*(11), 2467–2479. https://doi.org/10.1016/0016-7037(86)90030-X

Clague, D. A., Caress, D. W., Dreyer, B. M., Lundsten, L., Paduan, J. B., Portner, R. A., et al. (2018). Geology of the Alarcon Rise, Southern Gulf of California. *Geochemistry, Geophysics, Geosystems*, *19*, 807–837. https://doi.org/10.1002/2017GC007348

Clague, D. A., Dreyer, B. M., Paduan, J. B., Martin, J. F., Caress, D. W., Gill, J. B., et al. (2014). Eruptive and tectonic history of the Endeavour Segment, Juan de Fuca Ridge, based on AUV mapping data and lava flow ages. *Geochemistry, Geophysics, Geosystems*, *15*, 3364–3391. https://doi.org/10.1002/2014GC005415

Clague, D. A., Dreyer, B. M., Paduan, J. B., Martin, J. F., Chadwick, W. W. Jr., Caress, D. W., et al. (2013). Geologic history of the summit of Axial Seamount, Juan de Fuca Ridge. *Geochemistry, Geophysics, Geosystems*, *14*, 4403–4443. https://doi.org/10.1002/ggge.20240

Connelly, D. P., Copley, J. T., Murton, B. J., Stansfield, K., Tyler, P. A., German, C. R., et al. (2012). Hydrothermal vent fields and chemosynthetic biota on the world's deepest seafloor spreading centre. *Nature Communications*, *3*(1), 620. https://doi.org/10.1038/ncomms1636

Cook, T. L., & Stakes, D. S. (1995). Biogeological mineralization in deep-sea hydrothermal deposits. *Science*, *267*(5206), 1975–1979. https://doi.org/10.1126/science.267.5206.1975

Cruse, A. M., Seewald, J. S., Saccocia, P. J., & Zierenberg, R. A. (2008). Hydrothermal fluid composition at Middle Valley, northern Juan de Fuca Ridge: Temporal and spatial variability. In R. P. Lowell, J. S. Seewald, A. Metaxas, & M. R. Perfit (Eds.), *Magma to Microbe: Modeling Hydrothermal Processes at Ocean Spreading Centers, American Geophysical Union Monograph Series* (Vol. 178, pp. 145–166). Washington, DC. https://doi.org/10.1029/178GM08

DeMets, C., Gordon, R. G., & Argus, D. F. (2010). Geologically current plate motions. *Geophysical Journal International*, *181*(1), 1–80. https://doi.org/10.1111/j.1365-246X.2009.04491.x

Denlinger, R. P., & Holmes, M. L. (1993). A thermal and mechanical model for sediment hills and associated sulfide deposits along Escanaba Trough. In J. L. Morton, R. A. Zierenberg, & C. A. Reiss (Eds.) Geologic, hydrothermal, and biologic studies at Escanaba Trough. *Gorda Ridge, offshore northern California, U S Geological Survey Bulletin*, *2022*, 65–76.

Douville, E., Charlou, J. L., Oelkers, E. H., Bienvenu, P., Jove Colon, C. F., Donval, J. P., et al. (2002). The Rainbow Vent fluids (36°14′N, MAR): The influence of ultramafic rocks and phase separation on trace metal content in Mid-Atlantic Ridge hydrothermal fluids. *Chemical Geology*, *184*(1-2), 37–48. https://doi.org/10.1016/S0009-2541(01)00351-5

Edmond, J. M., Campbell, A. C., Palmer, M. R., Klinkhammer, G. P., German, C. R., Edmonds, H. N., et al. (1995). Time series studies of vent fluids from the TAG and MARK sites (1986, 1990) Mid-Atlantic Ridge: A new solution chemistry model and mechanism for Cu/Zn zonation in massive sulfide orebodies. In L. M. Parsons, C. L. Walker, & D. R. Dison (Eds.), *Hydrothermal vents and processes, Geological Society Special Publications* (Vol. 87, pp. 77–86). Geological Society, London.

Einsele, G., Gieskes, J. M., Curray, J., Moore, D. J., Aguayo, E., Aubry, M., et al. (1980). Intrusion of basaltic sills into highly porous sediments and resulting hydrothermal activity. *Nature*, *283*(5746), 441–445. https://doi.org/10.1038/283441a0

Francheteau, J., Needham, H. D., Choukroune, P., & Juteau, T. (1979). Massive deep-sea sulphide ore deposits discovered on the East Pacific Rise. *Nature*, *277*(5697), 523–528. https://doi.org/10.1038/277523a0

Friedman, I., & O'Neil, J. R. (1977). Compilation of stable isotope fractionation factors of geochemical interest. U.S. Geological Survey Professional Paper 440-KK.

Gallant, R. M., & Von Damm, K. L. (2006). Geochemical controls on hydrothermal fluids from the Kairei and Edmond vent fields, 23°–25°S, Central Indian Ridge. *Geochemistry, Geophysics, Geosystems*, 7, Q06018. https://doi.org/10.1029/2005GC001067

Goffredi, S., Johnson, S., Tunnicliffe, V., Caress, D., Clague, D., Escobar, E., et al. (2017). Hydrothermal vent fields discovered in southern Gulf of California clarify role of habitat in augmenting regional diversity. *Proceedings of the Royal Society B*, 284(1859). https://doi.org/10.1098/rspb.2017.0817

Hannington, M. D., de Ronde, C. E. J., & Petersen, S. (2005). Sea-floor tectonics and submarine hydrothermal systems. *Economic Geology*, 100, 111–141.

Hannington, M. D., Jonasson, I. R., Herzig, P. M., & Peterson, S. (1995). Physical and chemical processes of seafloor mineralization at mid-ocean ridges. In S. E. Humphris, R. A. Zierenberg, L. S. Mullineaux, & R. E. Thomson (Eds.), *Seafloor hydrothermal systems—Physical, chemical, biological and geological interactions, American Geophysical Union Monograph* (Vol. 91, pp. 115–157). Washington, DC.

Hodgkinson, M. R. S., Webber, A. P., Roberts, S., Mills, R. A., Connelly, D. P., & Murton, B. J. (2015). Talc-dominated seafloor deposits reveal a new class of hydrothermal system. *Nature Communications*, 6(1), 10150. https://doi.org/10.1038/ncomms10150

Humphris, S. E., Merzig, P. M., Miller, D. J., Alt, J. C., Becker, K., Brown, D., et al. (1995). The internal structure of an active sea-floor massive sulphide deposit. *Nature*, 377(6551), 713–716. https://doi.org/10.1038/377713a0

James, R. H., Elderfield, H., & Plamer, M. R. (1995). The chemistry of hydrothermal fluids from the Broken Spur Site, 29°N, Mid-Atlantic Ridge. *Geochimica et Cosmochimica Acta*, 59(4), 651–659. https://doi.org/10.1016/0016-7037(95)00003-I

Jamieson, J. W., Clague, D. A., & Hannington, M. D. (2014). Hydrothermal sulfide accumulation along the Endeavour Segment, Juan de Fuca Ridge. *Earth and Planetary Science Letters*, 395, 136–148. https://doi.org/10.1016/j.epsl.2014.03.035

Jamieson, J. W., Hannington, M. D., Clague, D. A., Kelley, D. S., Delaney, J. R., Holden, J. F., et al. (2013). Sulfide geochronology along the Endeavour Segment of the Juan de Fuca Ridge. *Geochemistry, Geophysics, Geosystems*, 14, 2084–2099. https://doi.org/10.1002/ggge.20133

Kelley, D. S., Karson, J. A., Blackman, D. K., Früh-Green, G. L., Butterfield, D. A., Lilley, M. D., et al., & the AT3-60 Shipboard Party (2001). An off-axis hydrothermal vent field near the Mid-Atlantic Ridge at 30°N. *Nature*, 412(6843), 145–149. https://doi.org/10.1038/35084000

Kelley, D. S., Karson, J. A., Fruh-Green, G. L., Yoerger, D. R., Shank, T. M., Butterfield, D. A., et al. (2005). A serpentinite-hosted ecosystem: The Lost City hydrothermal field. *Science*, 307(5714), 1428–1434. https://doi.org/10.1126/science.1102556

Kluesner, J. (2012). Marine geophysical study of cyclic sedimentation and shallow sill intrusion in the floor of the Central Gulf of California, 232 pages, unpublished Ph.D. dissertation, University of California, San Diego, Publication Number AAT 3487336.

Koski, R. A., Benninger, L. M., Zierenberg, R. A., & Jonasson, I. R. (1993). Composition and growth history of hydrothermal deposits in Escanaba Trough, southern Gorda Ridge. In J. L. Morton, R. A. Zierenberg, & C. A. Reiss (Eds.) Geologic, hydrothermal, and biologic studies at Escanaba Trough. *Gorda Ridge, Offshore Northern California, U S Geological Survey Bulletin*, 2022, 293–324.

Lilley, M. D., Butterfield, D. A., Lupton, J. E., & Olson, E. J. (2003). Magmatic events can produce rapid changes in hydrothermal vent chemistry. *Nature*, 422(6934), 878–881. https://doi.org/10.1038/nature01569

Lizarralde, D., Axen, G. J., Brown, H. E., Fletcher, J. M., Gonzales-Fernandez, A., Harding, A. J., et al. (2007). Variations in styles of rifting in the Gulf of California. *Nature*, 448(7152), 466–469. https://doi.org/10.1038/nature06035

Lonsdale, P. F., Bischoff, J. L., Burns, V. M., Kastner, M., & Sweeney, R. E. (1980). A high-temperature hydrothermal deposit on the seabed at a Gulf of California spreading center. *Earth and Planetary Science Letters*, 49(1), 8–20. https://doi.org/10.1016/0012-821X(80)90144-2

Lundsten, L., Reiswig, H. M., & Austin, W. C. (2014). Four new species of Cladorhizidae (Porifera, Demospongiae, Poecilosclerida) from the Northeast Pacific. *Zootaxa*, 3786(2), 101–123. https://doi.org/10.11646/zootaxa.3786.2.1

Lupton, J., Butterfield, D., Lilley, M., Evans, L., Nakamura, K.-I., Chadwick, Jr., W., Resing, J., et al. (2006). Submarine venting of liquid carbon dioxide on a Mariana Arc volcano. *Geochemistry, Geophysics, Geosystems*, 7, Q08007. https://doi.org/10.1029/2005GC001152

McDermott, J. M., Seewald, J. S., German, C. R., & Sylva, S. P. (2015). Pathways for abiotic organic synthesis at submarine hydrothermal fields. *Proceedings of the National Academy of Sciences*, 12, 7668–7672.

McDermott, J. M., Sylva, S. P., Ono, S., German, C. R., & Seewald, J. S. (2018). Geochemistry of fluids from Earth's deepest ridge-crest hot-springs: Piccard hydrothermal field, Mid-Cayman Rise. *Geochimica et Cosmochimica Acta*, 228, 95–118. https://doi.org/10.1016/j.gca.2018.01.021

Metz, S., & Trefry, J. H. (2000). Chemical and mineralogical influences on concentrations of trace metals in hydrothermal fluids. *Geochimica et Cosmochimica Acta*, 64(13), 2267–2279. https://doi.org/10.1016/S0016-7037(00)00354-9

Monecke, R., Petersen, S., Hannington, M. D., Grant, H., & Samson, I. (2016). The minor endowment of modern sea-floor massive sulfides and comparison with deposits hosted in ancient volcanic successions. *Reviews in Economic Geology*, 18, 245–306.

Mottl, M. J. (2012). VentDB: EPR21N. Mid-Ocean Ridge Hydrothermal Vent Chemistry Data Collection. https://doi.org/10.1594/IEDA/100208

Nakamura, K., Toki, T., Mochizuki, N., Asada, M., Ishibashi, J., Nogi, Y., et al. (2013). Discovery of a new hydrothermal vent based on an underwater, high-resolution geophysical survey. *Deep Sea Research, Part I*, 74, 1–10. https://doi.org/10.1016/j.dsr.2012.12.003

Ondréas, H., Scalabrin, C., Fouquet, Y., & Godfroy, A. (2018). Recent high-resolution mapping of Guaymas hydrothermal fields (Southern Trough). *Bulletin de la Societe Geologique de France - Earth Sciences Bulletin*, 189(1), 6. https://doi.org/10.1051/bsgf/2018005.

Palmer, M. R. (1991). Boron isotope systematics of hydrothermal fluids and tourmalines: A synthesis. *Chemical Geology (Isotope Geoscience Section)*, 94(2), 111–121. https://doi.org/10.1016/0168-9622(91)90004-G

Palmer, M. R., & Edmond, J. M. (1989). Cesium and rubidium in submarine hydrothermal fluids: Evidence for recycling of alkali elements. *Earth and Planetary Science Letters*, 95(1-2), 8–14. https://doi.org/10.1016/0012-821X(89)90163-5

Paull, C. K., Ussler, W. III, Peltzer, E. T., Brewer, P. G., Keaten, R., Mitts, P. J., et al. (2007). Authigenic carbon entombed in methane-soaked sediment from the northeastern transform margin of the Guaymas Basin, Gulf of California. *Deep-Sea Research Part III*, 54(11-13), 1240–1267. https://doi.org/10.1016/j.dsr2.2007.04.009

Peter, J., & Scott, S. (1988). Mineralogy, composition, and fluid inclusion microthermometry of sea-floor hydrothermal deposits in the southern trough of Guaymas Basin, Gulf of California. *Canadian Mineralogist*, 26, 567–587.

Peter, J. M., & Shanks, W. C., III (1992). Sulfur, carbon, and oxygen isotope variation in submarine hydrothermal deposits of Guaymas Basin, Gulf of California, USA. *Geochimica et Cosmochimica Acta*, 56(5), 2025–2040. https://doi.org/10.1016/0016-7037(92)90327-F

Piepgras, D. J., & Wasserburg, G. J. (1985). Strontium and neodymium isotopes in hot springs on the East Pacific Rise and Guaymas Basin. *Earth and Planetary Science Letters*, 72(4), 341–356. https://doi.org/10.1016/0012-821X(85)90057-3

Schmidt, K., Koschinsky, A., Gaarbe-Schönberg, D., de Carvalho, L. M., & Seifert, R. (2007). Geochemistry of hydrothermal fluid from the ultramafic-hosted Logatchev hydrothermal field, 15°N on the Mid-Atlantic Ridge: Temporal and spatial investigation. *Chemical Geology*, 242, 1–21.

Seal, R. R. II, & Hammarstrom, J. M. (2005). Chapter 2. Geoenvironmental models of mineral deposits: Examples from massive sulfide and gold deposits. In J. L. Jambor, D. W. Blowes, & A. I. M. Richie (Eds.), *Environmental aspects of mine waste*, *Short Course Series* (Vol. 31, pp. 11–50). Mineralogical Association of Canada, Quebec.

Seewald, J. S., Seyfried, W. E. Jr., & Shanks, W. C. III (1994). Variations in the chemical and stable isotope composition of carbon and sulfur species during organic rich sediment alteration: An experimental theoretical study Guaymas Basin. *Geochimica et Cosmochimica Acta*, *58*(22), 5065–5082. https://doi.org/10.1016/0016-7037(94)90232-1

Seyfried, W. E. Jr., Chen, X., & Chan, L.-H. (1998). Trace element mobility and lithium isotope exchange during hydrothermal alteration of seafloor weather basalt: An experimental study at 350°C and 500 bars. *Geochimica et Cosmochimica Acta*, *49*, 949–960.

Seyfried, W. E. Jr., Pester, N. J., Ding, K., & Rough, M. (2011). Vent fluid chemistry of the Rainbow hydrothermal system (36°N, MAR): Phase equilibria and in situ pH controls on subseafloor alteration processes. *Geochimica et Cosmochimica Acta*, *75*, 1574–1593.

Seyfried, W. E. Jr., Pester, N. J., Tutolo, B. M., & Ding, K. (2015). The Lost City hydrothermal system: Constraints imposed by vent fluid chemistry and reaction path models on subseafloor heat and mass transfer processes. *Geochimica et Cosmochimica Acta*, *163*, 59–79.

Shanks, W. C. III (2001). Stable isotopes in seafloor hydrothermal systems: Vent fluids, hydrothermal deposits, hydrothermal alteration, and microbial processes. In J. W. Valley & D. R. Cole (Eds.) Stable isotope geochemistry. *Reviews of Mineral Geochemistry*, *43*(1), 469–525. https://doi.org/10.2138/gsrmg.43.1.469

Simoneit, B. R. T., Kawka, O. E., & Brault, M. (1988). Origin of gases and condensates in the Guaymas Basin hydrothermal system (Gulf of California). *Chemical Geology*, *71*(1-3), 169–182. https://doi.org/10.1016/0009-2541(88)90113-1

Simoneit, B. R. T., Leif, R. N., Sturz, A. A., Sturdivant, A. V. E., & Gieskes, J. M. (1992). Geochemistry of shallow sediments in Guaymas Basin, Gulf of California: Hydrothermal gas and oil migration and effects of mineralogy. *Organic Geochemistry*, *18*(6), 765–784. https://doi.org/10.1016/0146-6380(92)90046-Z

Simoneit, B. R. T., Summerhayes, C. P., & Meyers, P. A. (1986). Sources and hydrothermal alteration of organic matter in Quaternary sediments: A synthesis of studies from the Central Gulf of California. *Marine and Petroleum Geology*, *3*(4), 282–297. https://doi.org/10.1016/0264-8172(86)90033-4

Soule, S., Seewald, J., Wankel, S., Michel, A., Beinart, R., Briones, E. E., et al. (2018). Exploration of the North Guaymas Basin. *Oceanography*, *31*(1), 39–41.

Spelz, R., Lupton, J., Evans, L., Zierenberg, R., Clague, D.A., Neumann, F., & Paduan, J. (2015). Noble gas geochemistry of the newly discovered hydrothermal fields in the Gulf of California: preliminary He-isotope ratios from the Alarcón Rise and Pescadero basin vent sites. Abstract OS23C-2028 Presented at the Fall AGU Meeting, San Francisco, CA, December 14–18.

Spiess, F. N., Macdonald, K. C., Atwater, T., Ballard, R., Carranza, A., Cordoba, D., et al. (1980). East Pacific rise: Hot springs and geophysical experiments. *Science*, *207*(4438), 1421–1433. https://doi.org/10.1126/science.207.4438.1421

Spivack, A. J., & Edmond, J. M. (1987). Boron isotope exchange between seawater and the oceanic crust. *Geochimica et Cosmochimica Acta*, *51*(5), 1033–1043. https://doi.org/10.1016/0016-7037(87)90198-0

Stein, C., Stein, S., & Pelayo, A. (1995). Heat flow and hydrothermal circulation. In S. Humphris, R. Zierenberg, L. Mullineaux, & R. Thomson (Eds.), *Physical, chemical, biological, and geological interactions within hydrothermal systems*, *American Geophysical Union Monograph* (Vol. 91, pp. 425–445). Washington, DC.

Tissot, B. P., & Welte, D. H. (1984). *Petroleum formation and occurrence* (2nd ed.). New York: Springer. https://doi.org/10.1007/978-3-642-87813-8

Tivey, M. K. (1995). The influence of hydrothermal fluid composition and advection rates on black smoker chimney mineralogy: Insights from modeling transport and reaction. *Geochimica et Cosmochimica Acta*, *59*(10), 1933–1949. https://doi.org/10.1016/0016-7037(95)00118-2

Tivey, M. K., Stakes, D. S., Cook, T. L., Hannington, M. D., & Petersen, S. (1999). A model for growth of steep-sided vent structures on the Endeavour Segment of the Juan de Fuca Ridge: Results of a petrologic and geochemical study. *Journal of Geophysical Research*, *104*, 22,859–22,883. https://doi.org/10.1029/1999JB900107

Trefry, J. H., Butterfield, D. B., Metz, S., Massoth, G. J., Trocine, R. P., & Feely, R. A. (1994). Trace metal in hydrothermal solutions from Cleft Segment on the Southern Juan de Fuca Ridge. *Journal of Geophysical Research*, *99*, 4925–4935. https://doi.org/10.1029/93JB02108

Von Damm, K. L. (1988). Systematics of and postulated controls on submarine hydrothermal solution chemistry. *Journal of Geophysical Research*, *93*, 4551–4561. https://doi.org/10.1029/JB093iB05p04551

Von Damm, K. L. (1990). Seafloor hydrothermal activity: Black smoker chemistry and chimneys. *Annual Review of Earth and Planetary Sciences*, *18*(1), 173–204. https://doi.org/10.1146/annurev.ea.18.050190.001133

Von Damm, K. L. (1995). Controls on the chemistry and temporal variability of seafloor hydrothermal fluids. In S. E. Humphris, R. A. Zierenberg, L. S. Mullineaux, & R. E. Thompson (Eds.), *Seafloor hydrothermal systems: Physical, chemical, biological, and geological interactions*, *American Geophysical Union Monograph* (Vol. 91, pp. 222–247). Washington, DC.

Von Damm, K. L. (2000). Chemistry of hydrothermal vent fluids from 9°–10°N, East Pacific Rise: "Time zero," the immediate posteruptive period. *Journal of Geophysical Research*, *105*, 11,203–11,222. https://doi.org/10.1029/1999JB900414

Von Damm, K. L., & Bischoff, J. L. (1987). Chemistry of hydrothermal solutions from the southern Juan de Fuca Ridge. *Journal of Geophysical Research*, *92*, 11,334–11,346. https://doi.org/10.1029/JB092iB11p11334

Von Damm, K. L., & Bischoff, J. L. (1991). Quartz solubility in hydrothermal seawater: An experimental study and equation describing quartz solubility for up to 0.5 M NaCl solutions. *American Journal of Science*, *291*(10), 977–1007. https://doi.org/10.2475/ajs.291.10.977

Von Damm, K. L., Bray, A. M., Buttermore, L. G., & Oosting, S. E. (1998). The geochemical controls on vent fluids from the Lucky Strike Vent Field, Mid-Atlantic Ridge. *Earth and Planetary Science Letters*, *160*(3-4), 521–536. https://doi.org/10.1016/S0012-821X(98)00108-3

Von Damm, K. L., Edmond, J. M., Grant, B., Measures, C. I., Walden, B., & Weiss, R. F. (1985). Chemistry of submarine hydrothermal solutions at 21°N, East Pacific Rise. *Geochimica et Cosmochimica Acta*, *49*(11), 2197–2220. https://doi.org/10.1016/0016-7037(85)90222-4

Von Damm, K. L., Edmond, J. M., Measures, C. I., & Grant, B. (1985). Chemistry of submarine hydrothermal solutions at Guaymas Basin, Gulf of California. *Geochimica et Cosmochimica Acta*, *49*(11), 2221–2237. https://doi.org/10.1016/0016-7037(85)90223-6

Von Damm, K. L., Oosting, S. E., Kozlowski, R., Buttermore, L. G., Colodner, D. C., Edmonds, H. N., et al. (1995). Evolution of East Pacific Rise hydrothermal vent fields following a volcanic eruption. *Nature*, *375*(6526), 47–50. https://doi.org/10.1038/375047a0

Von Damm, K. L., Parker, C. L., Zierenberg, R. A., Lilley, M. D., Olson, E. J., Clague, D. A., & McClain, J. S. (2005). The Escanaba Trough, Gorda Ridge hydrothermal system: Temporal stability and subseafloor complexity. *Geochimica et Cosmochimica Acta*, *69*(21), 4971–4984. https://doi.org/10.1016/j.gca.2005.04.018

Von Damm, K. L., Parker, C. M., Lilley, M. D., Clague, D. A., Zierenberg, R. A., Olson, E. J., & McClain, J. S. (2006). Chemistry of vent fluids and their implications for subsurface conditions at Sea Cliff hydrothermal field, Gorda Ridge. *Geochemistry, Geophysics, Geosystems*, *7*, Q05005. https://doi.org/10.1029/2005GC001034

Webber, A. P., Roberts, S., Murton, B. J., & Hodgkinson, M. R. S. (2015). Geology, sulfide geochemistry and supercritical venting at Beebe hydrothermal vent field, Cayman Trough. *Geochemistry, Geophysics, Geosystems*, *16*, 2661–2678. https://doi.org/10.1002/2015GC005879

Wessel, P. (2008). Global 30x30 arc sec relief blend, GMT Companion CD-ROM v2.0, Geoware-Online.com.

You, C.-F., Butterfield, D. A., Spivack, A. J., Gieskes, J. M., Gamo, T., & Campbell, A. J. (1994). Boron and halide systematic in submarine hydrothermal systems: Effects of phase separation and sedimentary contributions. *Earth and Planetary Science Letters*, *58*, 227–238.

Zierenberg, R., Shanks, W., & Bischoff, J. (1984). Massive sulfide deposits at 21°N, East Pacific Rise: Chemical composition, stable isotopes, and phase equilibria. *Geology Society of America Bulletin*, *95*(8), 922–929. https://doi.org/10.1130/0016-7606

Zierenberg, R. A., Clague, D. A., Paduan, J. B., & Caress, D. W. (2015). New maps Focusfocus 30-odd years of investigation of the Escanaba Trough spreading center, Geological Society of America Annual Meeting, Baltimore, Maryland, 1–4 November. *Abstracts with Programs*, *47*(7), 281.

Zierenberg, R. A., Fouquet, Y., Miller, D. J., Bahr, J. M., Baker, P. A., Bjerkgård, T., et al. (1998). The deep structure of a sea-floor hydrothermal deposit. *Nature*, *392*(6675), 485–488. https://doi.org/10.1038/33126

Zierenberg, R. A., Koski, R. A., Morton, J. L., & Bouse, R. M. (1993). Genesis of massive sulfide deposits on a sediment-covered spreading center, Escanaba Trough, Southern Gorda Ridge. *Economic Geology*, *88*(8), 2069–2098. https://doi.org/10.2113/gsecongeo.88.8.2069